iScience

CellPress
OPEN ACCESS

Article

Supracellular Actomyosin Mediates Cell-Cell Communication and Shapes Collective Migratory Morphology

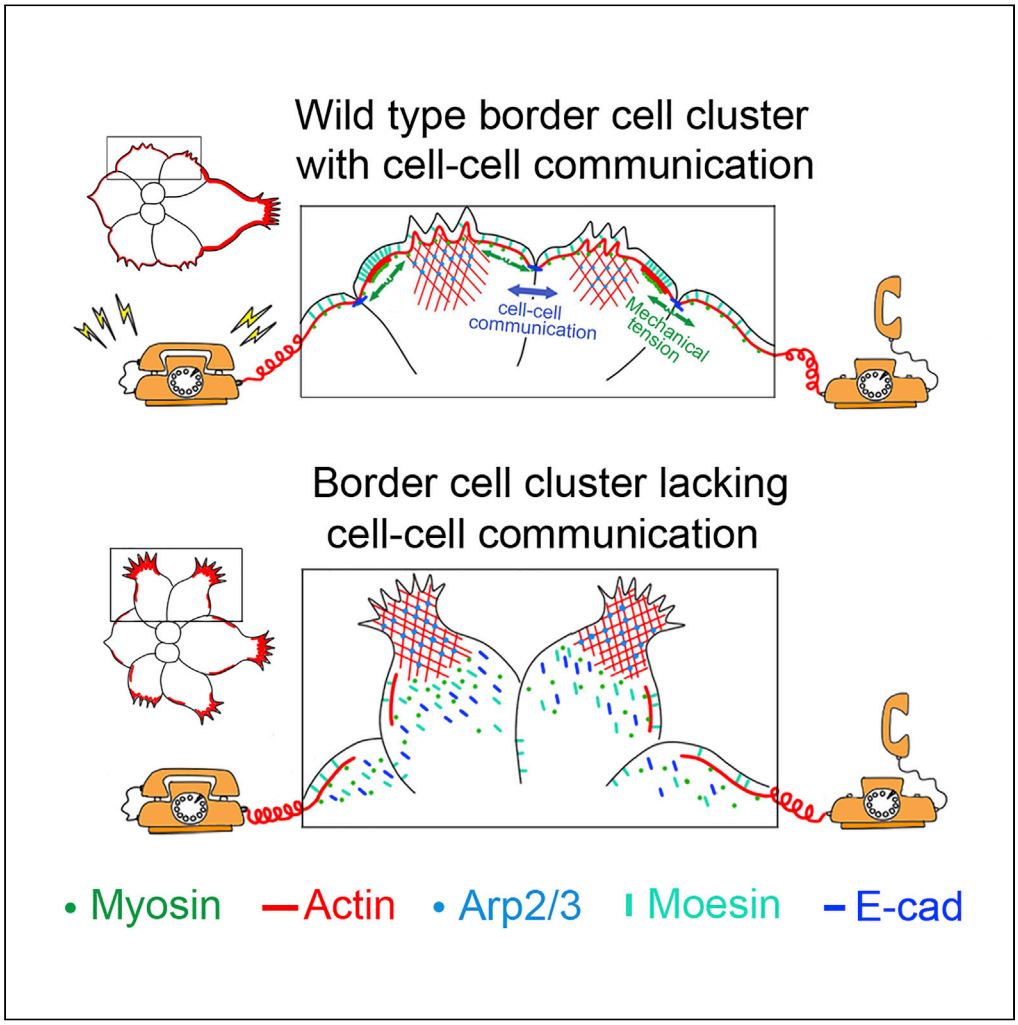

Heng Wang, Xuan Guo, Xianping Wang, Xiaobo Wang, Jiong Chen

wangheng@nicemice.cn (H.W.)
chenjiong@nju.edu.cn (J.C.)

HIGHLIGHTS

A supracellular actomyosin network encompasses the surface of migratory BC cluster

The network mediates cell-cell communication and restrains protrusion formation

Dynamics of myosin patches correlate with protrusion behaviors

A cytoplasmic dendritic actin population interacts with the actomyosin network

Wang et al., iScience *23*, 101204
June 26, 2020
https://doi.org/10.1016/j.isci.2020.101204

iScience

CellPress
OPEN ACCESS

Article

Supracellular Actomyosin Mediates Cell-Cell Communication and Shapes Collective Migratory Morphology

Heng Wang,[1,*] Xuan Guo,[1] Xianping Wang,[1] Xiaobo Wang,[2] and Jiong Chen[1,3,*]

SUMMARY

During collective cell migration, front cells tend to extend a predominant leading protrusion, which is rarely present in cells at the side or rear positions. Using *Drosophila* border cells (BCs) as a model system of collective migration, we revealed the presence of a supracellular actomyosin network at the peripheral surface of BC clusters. We demonstrated that the Myosin II-mediated mechanical tension as exerted by this peripheral supracellular network not only mediated cell-cell communication between leading BC and non-leading BCs but also restrained formation of prominent protrusions at non-leading BCs. Further analysis revealed that a cytoplasmic dendritic actin network that depends on the function of Arp2/3 complex interacted with the actomyosin network. Together, our data suggest that the outward pushing or protrusive force as generated from Arp2/3-dependent actin polymerization and the inward restraining force as produced from the supracellular actomyosin network together determine the collective and polarized morphology of migratory BCs.

INTRODUCTION

When individual cells undergo migration, they often extend a prominent lamellipodial protrusion at the leading edge while suppressing formation of large protrusions elsewhere. Such cell polarization is necessary for directional migration, as the leading protrusion is needed for direction sensing, substrate adhesion, and forward movement (Devreotes and Janetopoulos, 2003). In comparison, during collective migration of a coherent group of cells, large actin-rich lamellipodial protrusions are mostly extended by cells at the front position (but not at the side or back positions) of the group (Friedl and Gilmour, 2009; Mayor and Etienne-Manneville, 2016; Montell et al., 2012). But the underlying mechanism for the generation of such front-polarized morphology is not clear. A recent study done in cultured epithelial cells in a two-dimensional (D) environment demonstrated that the polarized morphology depends on a network of supracellular actomyosin bundles that constrains the lateral side of the migratory cell group. The contractile force provided by Myosin II that is activated by Rho signaling is thought to suppress the formation of non-leading protrusions by cells at the lateral side (Friedl et al., 2014; Reffay et al., 2014). However, whether similar supracellular actomyosin structure exists in collectively migrating cell groups *in vivo* in a 3D environment is not clear.

An important feature of collective migration is that migratory cells remain connected via various cell-cell linkages, including tight junctions and adherens junctions, throughout the migratory process (Friedl and Gilmour, 2009). Conceivably, these cells can communicate and coordinate with each other to affect the collective behavior and morphology of the entire group (Etienne-Manneville, 2014; Mayor and Etienne-Manneville, 2016). But by what means the cells communicate with one another (i.e., via signaling peptides, small molecules, or mechanical means) and how cell-cell communication affect the collective behavior are largely unknown.

The border cells (BCs) in *Drosophila* ovary provide an excellent *in vivo* model for studying both the front-back polarity and cell-cell communication during collective migration (Montell et al., 2012). The migratory cluster of about eight BCs is derived from the follicle epithelium, which is a somatic monolayer encircling developing egg chambers (Figure 1A). During stage 9 of oogenesis, the BC cluster delaminates from the anterior follicle epithelium, invades the underlying germ-line tissue of nurse cells, and migrates posteriorly

[1]State Key Laboratory of Pharmaceutical Biotechnology and MOE Key Laboratory of Model Animals for Disease Study, Model Animal Research Center, Nanjing University, 12 Xue-fu Road, Nanjing 210061, China

[2]LBCMCP, Centre de Biologie Integrative (CBI), Universite de Toulouse, CNRS, UPS, 31062 Toulouse, France

[3]Lead Contact

*Correspondence: wangheng@nicemice.cn (H.W.), chenjiong@nju.edu.cn (J.C.)

https://doi.org/10.1016/j.isci.2020.101204

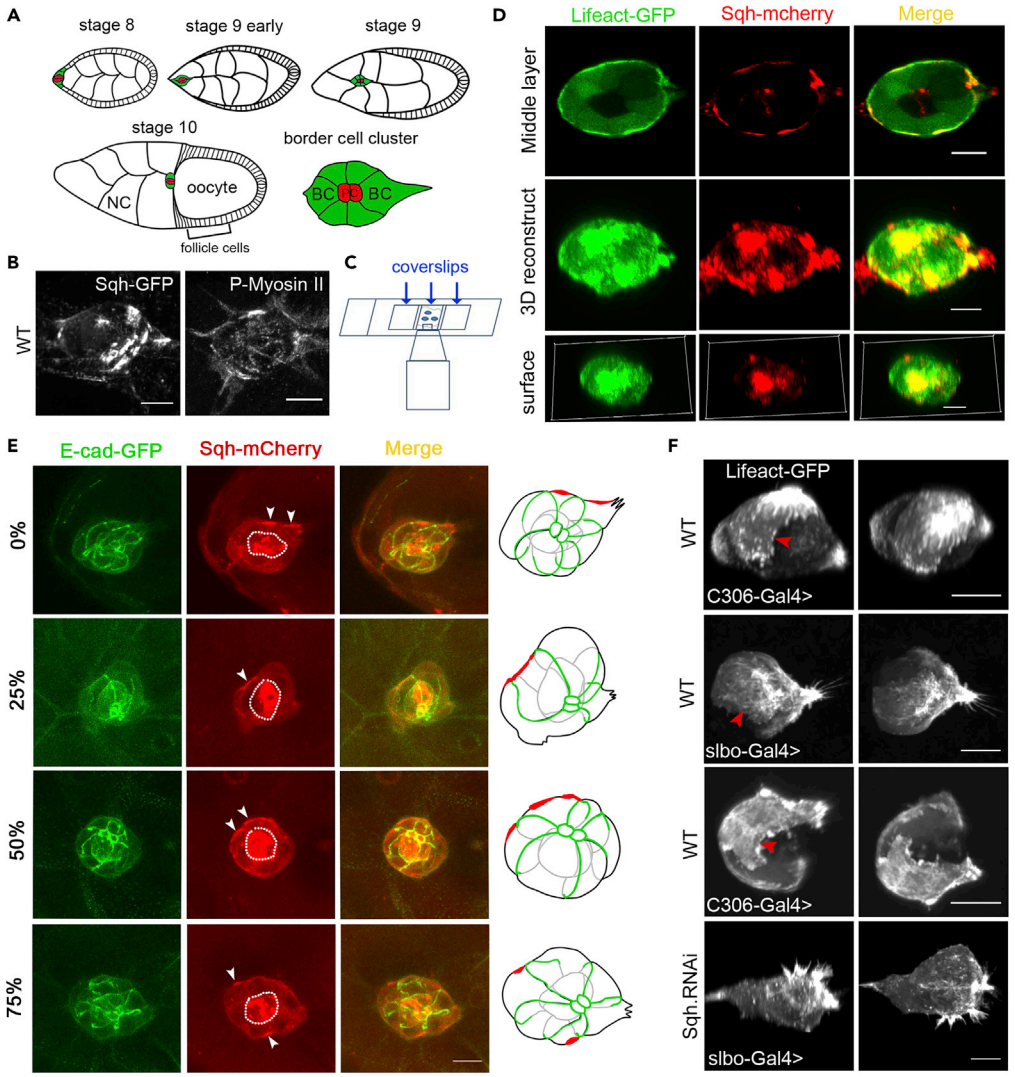

Figure 1. Presence of a Supracellular Actomyosin Network on the Surface of BC Clusters

(A) Diagram of cluster formation, delamination, and collective migration of BCs. NC, nurse cells; BC, border cells (green); PC, polar cells (red).

(B) Wild-type BCs labeled with Sqh-GFP (left) and P-Myosin II antibody (right).

(C) Schematic diagram of imaging egg chambers that were mounted with two bridges (coverslips) between a slide and a coverslip (see Transparent Methods).

(D) Confocal images of BC clusters showing distribution pattern of F-actin (represented by Lifeact-GFP) and Myosin II (represented by Sqh-mCherry). A middle section taken out of a confocal z series shows that F-actin and Myosin II colocalize in the periphery of BC cluster (first row). 3D reconstruction of the z series further demonstrates that F-actin and Myosin II colocalize as large patches on the surface of the same BC cluster (second row and third row).

(E) Representative images of migratory BC clusters at various migratory positions (0%, 25%, 50%, 75%; see "Quantification of BC migration" in Transparent Methods), showing distribution pattern of E-cadherin (represented by E-cad-GFP) and Myosin II (represented by Sqh-mCherry). Images are derived from maximum projection of confocal z series; schematic diagrams are shown to the right. White arrowheads point to Myosin II patches on the surface, white dotted line outlines the central polar cells.

(F) High-resolution images (viewed at different angles after rotation), as resulted from 3D reconstruction, display a continuous F-actin network present on the surface (indicated by red arrowheads). F-actin was labeled by Lifeact-GFP that was expressed using a *C306-Gal4* or *slbo-Gal4* driver. *sqh RNAi* resulted in disruption of the continuous F-actin network on the surface of BC cluster. F-actin level was reduced and its organization became random. Furthermore, ectopic protrusions were formed. For all images of BC clusters in this and all subsequent figures, migration direction is to the right unless indicated otherwise. Scale bars: 10 μm.

See also Figure S1 and Videos S1 and S2.

between nurse cells in a 3D environment until reaching the border between nurse cells and the oocyte, hence the name border cells. During BC migration, a prominent actin-rich protrusion is observed to be extended by one or two BCs at the front or leading position of cluster throughout the migratory process, and such large protrusions are rarely found at the non-leading (side and back) positions (Veeman and McDonald, 2016; Zhang et al., 2011). Although it is known that the RTK (receptor tyrosine kinase) signaling from the guidance receptor PVR directs the chemotactic migration of BCs and results in the overall front-back polarity of the cluster (Poukkula et al., 2011), how the formation of large protrusions is suppressed at non-leading positions and how the front polarized morphology of BC cluster is maintained are much less understood. Interestingly, recent reports studying BC migration indicated that this polarized morphology is affected by cell-cell communication. Employing a photoactivatable form of Rac (PA-Rac), it was demonstrated that inducing an ectopic protrusion at the rear cell of BC cluster led to the retraction of prominent protrusion at the front cell, effectively reversing the front-back polarity and migration direction (Wang et al., 2010). This and other subsequent studies using this optogenetic approach demonstrated that front BCs can communicate with BCs at the side and rear positions to coordinate the collective morphology and migration of BC clusters. Furthermore, these studies showed that this form of cell-cell communication requires JNK signaling, E-cadherin, Rab11, Moesin, and Cdc42 (Cai et al., 2014; Ramel et al., 2013; Wang et al., 2010). But how and by what means the BCs communicate with each other are still not clear.

In this study, we reveal the presence of a supracellular actomyosin network on the peripheral surface that encompasses the entire BC cluster. We find that this actomyosin network that depends on Myosin II and Rho signaling functions to suppress the formation of ectopic protrusion at non-leading positions of BC clusters. Furthermore, we find that this supracellular actomyosin network mediates effective cell-cell communication, since local disruption of the network with genetic and optogenetic means abolishes communication between BCs.

RESULTS

Superacellular Actomyosin Network Encompasses the Surface of BC Cluster

Myosin II had been shown to be essential to delamination and collective migration of BCs (Majumder et al., 2012). A recent study further demonstrated that it promotes cortical tension to maintain BC cluster morphology and resist compressive force from nurse cells (Aranjuez et al., 2016). Myosin II was also shown to be highly expressed in BCs and often enriched in foci at the cluster periphery (Aranjuez et al., 2016; Combedazou et al., 2017; Majumder et al., 2012). Nevertheless, a detailed spatial relationship between Myosin II and actin cytoskeleton and the high-resolution morphology of actomyosin network within BCs have not been clearly described. To achieve these objectives, we first used a Sqh-GFP (encoding Myosin II's regulatory light chain) transgene, which is expressed by a *sqh* promoter, and a Phospho-Myosin light chain antibody (P-Myosin II) to visualize Myosin II and its active form, respectively (Majumder et al., 2012; Royou et al., 2004). Consistent with previous reports, both Sqh-GFP and P-Myosin II were found to be enriched in cortical patches or foci at cluster periphery (Figure 1B) (Majumder et al., 2012). Previous studies have shown that actin filaments (F-actin) displayed a polarized distribution at the outer periphery of BC cluster (Lucas et al., 2013). To describe the spatial relationship between Myosin II and F-actin, we used *slbo-Gal4* or *C306-Gal4* to specifically drive the expression of Lifeact-GFP (labeling F-actin) (Riedl et al., 2008) in BCs that also express Sqh-mCherry (labeling Myosin II [Martin et al., 2009; Qin et al., 2018; Qin et al., 2017]) by a *sqh* promoter from a genomic fragment. In a cross-sectional view of BC cluster, high levels of F-actin encircled and accumulated at the periphery of cluster, whereas Myosin II strongly colocalized with some of the F-actin "segments" and "foci" at the outer periphery (Figure 1D, first row). 3D reconstruction using z series of confocal sections revealed that Myosin II and F-actin strongly colocalized in large patches on the surface of BC clusters, with the area of F-actin patches generally larger than that of Myosin II (Figure 1D, second and third rows). Besides the peripheral localization, Myosin II was also localized more internally within the BC cluster, showing a strong enrichment in the central polar cells but only a mild distribution in the cell-cell junctions that were labeled by E-cadherin (Figure 1E; Video S1).

To obtain high-resolution details of actin network on the surface of BC cluster, we employed a form of confocal microscopy close to super-resolution (see Transparent Methods). A z series of confocal sections thus captured was used for 3D reconstruction to better reveal the actin cytoskeleton. Additionally, we also modified the protocol for mounting egg chambers during confocal viewing to avoid distortion or compression of BC cluster in the z axis (Figure 1C). Lastly, to obtain better contrast between surface F-actin network and internal F-actin, we selected BC clusters that displayed mosaic expression of Lifeact-GFP due to the

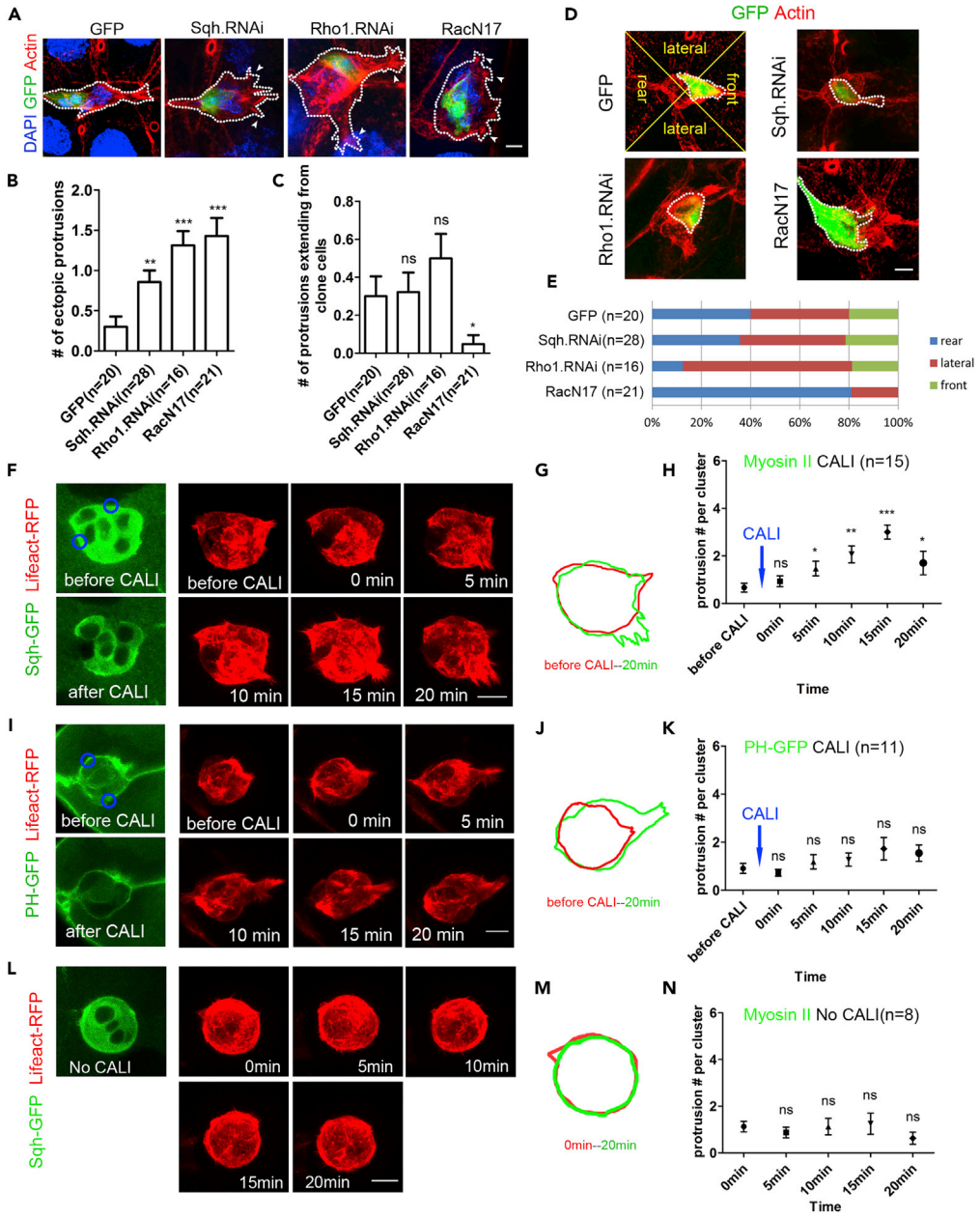

Figure 2. Local Inactivation of Sqh, Rho1, and Rac Results in Non-autonomous Formation of Ectopic Protrusions

(A) Ectopic protrusions were present in mosaic BC clusters containing single cell clones expressing *sqh RNAi*, *rho1 RNAi*, or *RacN17*. The *Ay-Gal4/UAS-GFP, UAS*-transgene generated a flip-out clone co-expressing the transgene along with GFP, which labeled the single cell clones within the otherwise wild-type clusters. Dotted lines outline the BC clusters. Mosaic BC clusters containing single-cell clones that express GFP only were used as controls. White arrowheads indicate ectopic protrusions.

(B) Average number of ectopic or non-leading protrusions for each mosaic cluster (containing single cell clones) was quantified.

(C) Quantification of the average number of protrusions extending from each single cell clone.

(D) Four mosaic BC clusters containing *GFP*, *sqh RNAi*, *rho1 RNAi*, and *RacN17* expressing single cell clones, respectively. *GFP*, *sqh RNAi*, and *rho1 RNAi* expressing single-cell clones are located at the front position, RacN17 expressing clone is at the back or rear position. Dotted lines mark the single cell clones.

(E) Mosaic BC clusters were scored for the percentage of the GFP-labeled single cell clones that are present in the front, lateral, or rear positions. RacN17 expression in single cell clones biased them to become the lagging cells within the mosaic clusters.

Figure 2. *Continued*

(F) Ectopic protrusions were formed after CALI of Sqh-GFP. Lifeact-RFP is expressed by *slbo-Gal4* to label F-actin. Two blue circles indicate regions of illumination.

(G) Alignment of BC cluster peripheries reveals the ectopic protrusions (red periphery: before CALI; green periphery: 20 min after CALI).

(H) Quantification of protrusions per BC cluster at different time points of the CALI experiment. A significant increase of protrusion number is shown 5 min after CALI treatment (n = 15 BC clusters).

(I) Ectopic protrusions were not formed after CALI of PH-GFP.

(J) Alignment of BC cluster peripheries reveals no ectopic protrusion formation.

(K) Quantification of protrusions shows no significant difference between time points after CALI of PH-GFP (n = 11).

(L–N) Live imaging of Sqh-GFP and Lifeact-RFP expressing BC cluster without CALI treatment. These BC clusters are used as the "no CALI" control for (F)–(K).

*, <0.05; **, $p < 0.01$; ***, $p < 0.001$; ns, not significant (Student's t test); Data are represented as mean ± SEM. Scale bars: 10 μm. See also Figures S1 and S2 and Video S3.

occasionally non-uniform Gal4 expression from *slbo-Gal4* and *c306-Gal4* drivers (Figure 1F; Video S2; Figure S1A). The resulting high-resolution images from 3D confocal reconstruction confirmed the existence of F-actin patches of high intensity on the surface of BC clusters (Figure 1F, first row). Furthermore, a population of F-actin at medium intensity also exists more ubiquitously as a continuous network on the surface (Figure 1F, indicated by red arrowheads), in contrast to the low level of F-actin in the more internal cytoplasm (Figure 1F). Finally, a single large actin-rich protrusion was usually seen at the leading position, whereas a few minor protrusions could sometimes be seen at the side of BC clusters (Figure 1F, second row). To explore whether the structure of F-actin patches and a uniform and continuous network of F-actin depend on Myosin II, we expressed *sqh RNAi* with *slbo-Gal4* to knock down Sqh's function. Strikingly, the F-actin network along with patches as appeared in the wild-type BC clusters was disrupted after *RNAi* expression. We observed random spots of F-actin without extensive connection or networking among them on the surface of BC clusters (Figure 1F, fourth row; Video S2). In addition, large ectopic protrusions were also observed in *sqh RNAi* BCs. Together, these results demonstrate that Myosin II and F-actin form large patches or foci on the surface of clusters, which depend on Myosin II's function. Importantly, high-resolution imaging revealed the presence of a distinct F-actin network that depends on Myosin II. It is interesting that such an F-actin network appears to be ubiquitous and continuous throughout the cluster surface (Figure 1F, second and third rows), suggesting that Myosin II could exert its contractile force on a supracellular actin network to influence a collective cluster morphology. Indeed, reduction of Myosin II resulted in substantial changes in cluster morphology, turning a polarized cluster with a prominent leading protrusion into a less polarized cluster with multiple large protrusions at non-leading positions (Figure 1F).

Local Inactivation of Rho and Rac Results in Non-autonomous Changes on Collective Morphology

If the hypothesis of a supracellular actomyosin structure mediating collective mechanical tension on the entire cluster is correct, then a global change in cluster morphology may occur if we disrupt actomyosin network locally in only one BC. Under this assumption, a local break will loosen the global tension. We first employed a genetic approach by using the flip-out technique (del Valle Rodriguez et al., 2011) to reduce the Myosin II activity and actin polymerization, respectively, in a single BC within an otherwise wild-type cluster. *sqh RNAi*, *rho1 RNAi*, or dominant negative form of Rac1 (RacN17) was expressed in single cell clones within the mosaic clusters. Wild-type BC clusters typically display a polarized cluster morphology. In contrast, we found that mosaic BC clusters that contained *sqh RNAi* or *rho1 RNAi* expressing single cell clones displayed a less polarized morphology, with increased number of ectopic protrusions extending around the cluster, both from the non-clone cells and clone cells (Figures 2A–2D). This phenotype was not due to disruption of apical polarity proteins, because Par3/Baz and aPKC were still distributed in a wild-type pattern in clusters with reduced levels of Rho1 (Figures S1B and S1C). Intriguingly, expressing *RacN17* (at 29°C) in single cell clones also rendered the mosaic BC clusters extending ectopic protrusions (Figures 2A, 2B, and 2D). But different from the *sqh RNAi* and *rho1 RNAi* results, most of the *RacN17* clones did not extend protrusions themselves (Figures 2A–2C). Consistent with Rac's protrusion formation role, 0% of *RacN17* single cell clones were found in the front position of mosaic clusters in contrast to 20% for *GFP*, 21.4% for *sqh RNAi*, and 18.8% for *rho1 RNAi*, indicating that Rac promotes leader cell's protrusion and hence its migratory ability (Figures 2D and 2E). Together, our findings indicate that reducing Myosin II's contractile activity or lowering actin polymerization locally in single BCs each results in non-autonomous and global changes in overall cluster morphology. Since Sqh (or Rho1) and Rac1 may affect two different

aspects of the same actomyosin network, the similar non-autonomous changes from both experiments probably resulted from the disruption of the proposed supracellular network. On the other hand, the difference in protrusion extension by single cell clones between *rho1 RNAi* and *RacN17* suggests that Rho1 and Rac have different autonomous roles in promoting protrusion formation.

Local Inactivation of Myosin II by CALI Results in Non-autonomous Changes on Collective Morphology

Owing to the low spatial-temporal resolution of the genetic flip-out technique, we undertook an optogenetic approach to directly and locally inhibit Myosin II's function in BCs. Chromophore-assisted laser inactivation (CALI) uses intense laser to illuminate a chromophore, including GFP, to produce toxic reactive oxygen species that can damage a targeted protein within close proximity (Jacobson et al., 2008; Sano et al., 2014). CALI of Myosin II's regulatory light chain has been used successfully in inactivation of Myosin II in *C. elegans* Q neuroblast lineage division or in cell sorting at the compartmental boundaries in *Drosophila* embryos (Monier et al., 2010; Ou et al., 2010). We first tested whether we could use CALI (see Transparent Methods) to inhibit detachment of BCs from the anterior follicle epithelium, a process that was previously shown to require Myosin II function (Majumder et al., 2012). Repeated laser illumination of Sqh-GFP (5-s laser illumination for three or four times) at the rear side of BC cluster inhibited its efficient detachment (Figures S2A, second row, S2B, and Video S3). But such inhibition of detachment did not occur without illumination (Figure S2A, first row) or with illumination targeting PH-GFP, a PIP3 reporter that displays similar distribution as Sqh-GFP and composed of pleckstrin-homology (PH) domain of Grp1 fused to GFP (Figures S2A, third row, S2B, and Video S3) (Britton et al., 2002; Pickering et al., 2013). These results validate the effectiveness of CALI on inhibiting Sqh's function and thus Myosin II's activity in BCs. Next, we applied CALI (5-s illumination for eight times) to the lateral sides of BCs and then tracked the morphological change of cluster after CALI treatment by capturing confocal images every 5 min. Normally, migratory BCs only extend a single predominant protrusion from the front cell (Figure 2F) (Zhang et al., 2011). In contrast, BCs after CALI treatment extended large ectopic protrusion(s) elsewhere, at different positions of the cluster, and this morphological change could be detected 5 min after CALI. Fifteen minutes later, the number of ectopic protrusions reached maximum (Figures 2F–2H). To avoid nonspecific effects, we also performed similar experiments with no CALI treatment or with CALI of PH-GFP and found no significant formation of ectopic protrusions (Figures 2I–2N). Our results indicate that direct and local inhibition of Myosin II function by CALI also resulted in non-autonomous changes on the collective cluster morphology of BCs, further confirming the presence of a supracellular actomyosin network that exerts its contractile force on the entire cluster.

Dynamics of the Actomyosin Network

Next, we sought to further characterize the dynamics of the supracellular actomyosin network. We first documented the dynamics of Myosin II (Sqh-GFP) patches on the peripheral surface of BC cluster at four different stages or time points of its migration: at 0% (initiation of migration), at 25% (early migratory phase), at 75% (late migratory phase), and at 100% (end of migration, reaching the border). Owing to restriction in the scanning speed of confocal microscopy, we were only able to capture a z series encompassing the whole BC cluster every 20 or 30 s for the live imaging (Figure S3 and Video S4). With such temporal resolution, we observed a highly dynamic movement of Myosin II patches on the peripheral surface as the BCs initiated (at 0%) and undertook migration during early (at 25%) and late (at 75%) phases, respectively (Figure S3 and Video S4). In contrast, much less dynamic movement of Myosin II patches was observed for BCs that had terminated the posterior migration (at 100%), suggesting that dynamic movement of Myosin II patches may play important roles in active BC migration. In order to obtain finer details of the dynamic movement, we then focused on five sub-regions on the surface of migratory BC cluster, including rear side (1), lateral side (2), front side that does not contain protrusion (3), leading protrusion (4), and lateral protrusion (5). Live imaging with Sqh-GFP and Lifeact-RFP revealed that the first three sub-regions (1–3) exhibited a similar uni-directional movement or flow of Myosin II patches along the outer cortex of BC at various positions (Figures 3A–3C, S4A, and S4B, and Video S5). Interestingly, live imaging of leading protrusions revealed that single flow or multiple flows of Myosin II patches accompanied a simultaneous retraction of leading protrusion (Figures 3D and 3E; Video S6). Specifically, we observed three distinct types of patch movement upon further analysis. First, a majority of samples (10 of 18) displayed flows of Myosin II patches from the base of protrusion toward the tip of protrusion while the protrusion retracted (Figures S4C and S4D). Second, a small proportion of samples (3 of 18) exhibited flows of Myosin II patches that initiated near the tip and moved toward the base of protrusion (Figures S4E and S4F). Third, a significant

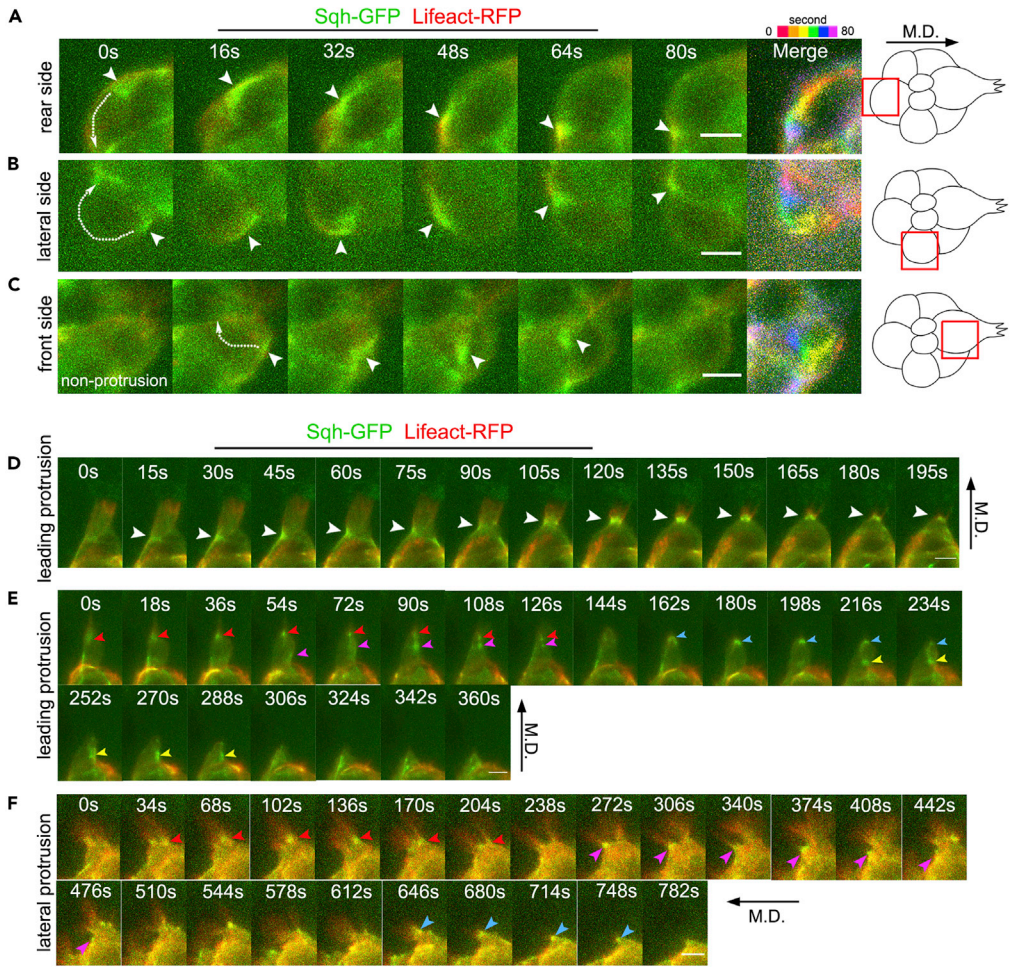

Figure 3. The Dynamics of Myosin II in Migratory BCs

(A–C) Selected still images from time-lapse movies showing highly dynamic movement or flow of Myosin II patches on BC cluster's peripheral surface at the rear side (A), lateral side (B), and front side (C), which do not contain protrusions. Sqh-GFP labels Myosin II and Lifeact-RFP labels F-actin. Arrowheads indicate Myosin II patches. Curved arrows indicate direction of Myosin II patches' movement. The polychromatic images in the rightmost panels display the motion trails of Myosin II patches. Red square boxes in schematic diagrams indicate the position of each sub-region within the BC cluster. M.D. and black arrow indicate migratory direction.

(D and E) Time-lapse images showing a single flow (D) or multiple flows (E) of Myosin II patches toward the tip of leading protrusion during a simultaneous retraction of leading protrusions.

(F) Time-lapse images showing the formation and movement of multiple Myosin II patches in the lateral protrusion during protrusion's retraction. Arrowheads of each color indicate a separate Myosin II flow. Scale bars: 5 μm.

See also Figures S3–S5 and Videos S4, S5, and S6.

minority of cases (5 of 18) indicated that Myosin II patches beginning at the base of protrusion first flowed toward the tip and then moved back toward the base as the protrusion retracted (Figures S4G and S4H). Together, these results suggest that the Myosin II flows are responsible for protrusion retraction, consistent with the idea that the actomyosin network acts to restrict protrusion. Similarly, formation and movement of multiple Myosin II patches in the lateral protrusions seem to correlate with retraction of lateral protrusions (Figure 3F and Video S6). Together, these results demonstrate that the actomyosin network on the surface of BC cluster displays a dynamic distribution during collective migration and that the movement of Myosin II patches closely correlate with the retraction of protrusions.

We then proceeded to further characterize the different forms of Myosin II organization and determine how each form of organization affects protrusion. We found that large clusters or aggregates of Sqh-GFP (on the surface of the entire BC cluster), which we referred to as "patches," tend to negatively correlate with

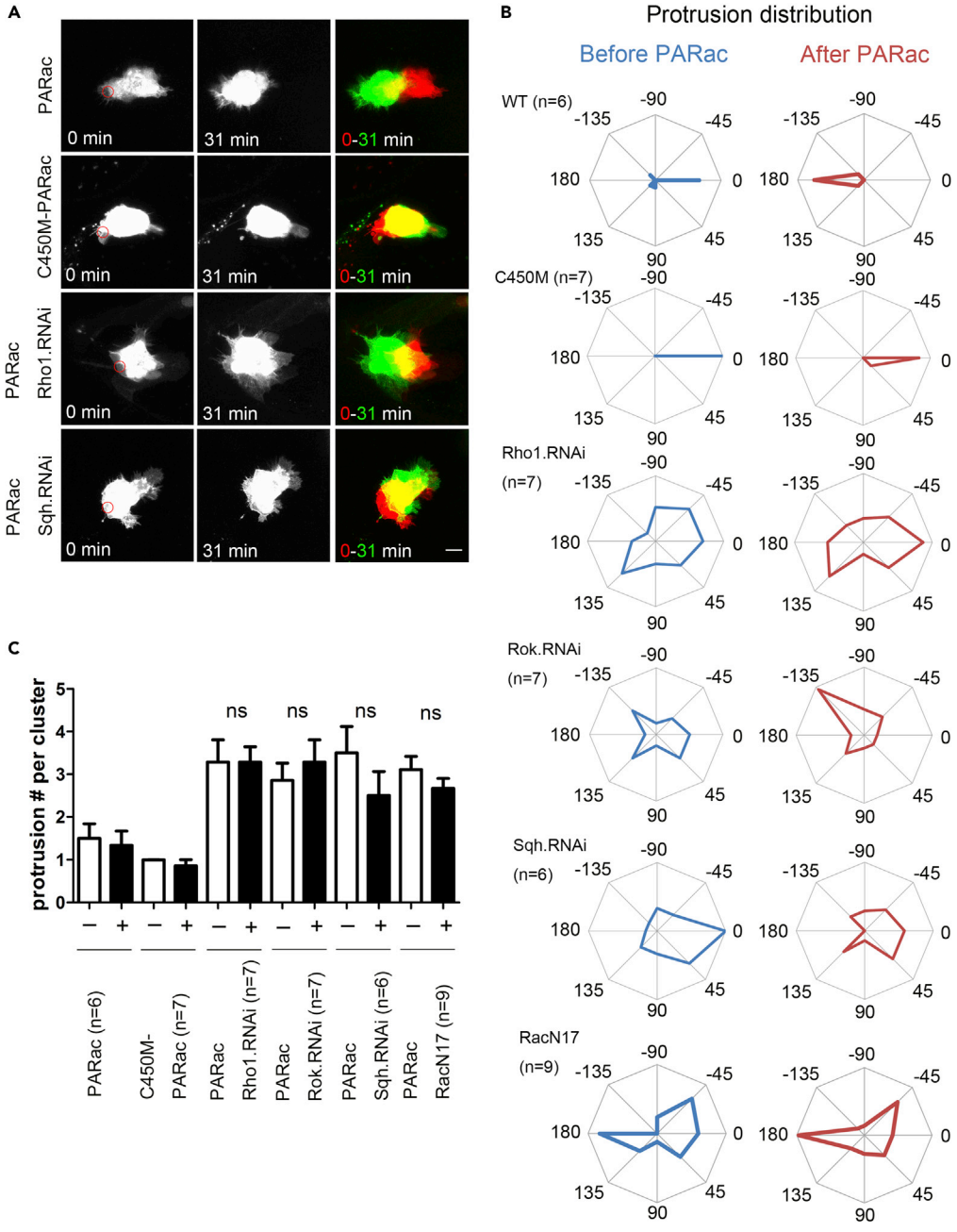

Figure 4. Loss of Function of Rho1, Rok, Sqh, and Rac Disrupts Cell-Cell Communication

(A) Confocal images in the top row show that local activation of PA-Rac in the rear of BCs induces a new protrusion and causes the original leading protrusion to retract in 31 min, demonstrating efficient cell-cell communication between front and rear cells. The second row shows the negative control with a photo-insensitive C450M-PA-Rac, where leading protrusion fails to retract 31 min after laser illumination at the rear region of BC cluster. The third and fourth rows demonstrate the effect of local photoactivation of PA-Rac in *rho1 RNAi* (third row) or *sqh RNAi* (fourth row) expressing BCs. The small red circles indicate regions of photoactivation.

(B) Analysis of protrusion distribution by the radar diagram, which divides the BC cluster into eight sectors. In the wild-type (WT) control clusters, most of protrusions were aligned toward 0° (front) before PA-Rac photoactivation but were switched toward 180° (rear) after photoactivation. Such a switch in protrusion distribution pattern did not occur in the C450M negative controls as well as in the *rho1 RNAi*, *rok RNAi*, *sqh RNAi*, and RacN17-expressing BCs. The expression was driven by *slbo-Gal4* at 29°C except for RacN17 (at 25°C).

Figure 4. *Continued*

(C) Quantification of average protrusion number per cluster shows no significant reduction of protrusion number between before photoactivation (−) and after photoactivation (+), indicating a lack of retraction of ectopic protrusions at the front or lateral positions of BC clusters. ns, not significant (Student's t test); data are represented as mean ± SEM. Scale bar:10 μm.

formation of large protrusion. Specifically, the larger and more numerous the Sqh-GFP patches are, the smaller the leading protrusion becomes (Figures S5A–S5C). We also found that the small aggregates of Sqh-GFP that were dispersed throughout the peripheral surface, which we referred to as "spots," tend to positively correlate with large protrusions (Figures S5D, S5E, and S5G). Our data showed that photoactivation of Rac in the leading BC that initially contained a small protrusion resulted in the marked increase of protrusion size (within a few minutes), which is accompanied by the significant increase of Myosin II spots and reduction of Myosin II patches (Figures S5D, S5E, S5G, and S5H). Conversely, retraction of a large leading protrusion by Rac photoactivation in the rear BC via cell-cell communication (see below section for more details) resulted in less Myosin II spots and more Myosin II patches (Figures S5F; 6 of 7 BC clusters). Together, these results suggest that different Myosin II organizations could correlate with or regulate different morphological changes such as protrusion extension or retraction.

Local Photoactivation of Rac Reveals that Rho/Rok/Myosin II Play Roles in Cell-Cell Communication

It was previously shown that the BC cluster displayed cell-cell communication between the leading cell and other non-leading cells (Cai et al., 2014; Ramel et al., 2013; Wang et al., 2010), but the underlying mechanism was not clear. Our results suggest that the proposed superacellular actomyosin network could mediate such cell-cell communication. To further test this idea, we determine whether cell-cell communication could be disrupted by loss of function of Rho, Rok, Sqh, and Rac, which supposedly are critical for the integrity of the actomyosin network and were shown here to be non-autonomously required for the collective cluster morphology. Previously, cell-cell communication among BCs was assayed by the PA-Rac system, which employed the photoactivatable form of Rac (PA-RacQ61L) (Wang et al., 2010). In the wild-type control, illumination of blue laser light at non-leading positions could cause a dramatic effect of leading protrusion retraction and extension of an ectopic protrusion at the site of illumination, effectively demonstrating the cell-cell communication between leading cell and non-leading cells. On the contrary, loss of function of JNK (involved in cell-cell adhesion), E-cadherin, Moesin (a component of actin cytoskeleton), and Rab11 (supposedly involved in transport of Moesin) was previously shown to result in failure of protrusion retraction and thus ineffective communication (Cai et al., 2014; Ramel et al., 2013; Wang et al., 2010). Here, we show that, within the cluster of control BCs expressing PA-Rac (using the *slbo-Gal4* driver), illumination and thus activation of exogenous Rac at the rear leads to induced protrusion at the rear and retraction of leading protrusion, indicating that the leading cell, which is at least one cell distance away, somehow sensed the communication from the rear BC and retracted its protrusion within 31 min (Figure 4A, first row; quantified in Figures 4B and 4C). But the light insensitive form of PA-Rac (C450M-PA-RacQ61L) lacked such effects (Figure 4A, second row; quantified in Figures 4B and 4C). Importantly, we found that photo-activation of Rac at the rear of *Sqh RNAi* expressing BC clusters did not cause protrusion retraction in cells at other positions (Figure 4A, fourth row; quantified in Figures 4B and 4C), even though the rear cell still formed induced protrusion (from activation of exogenous PA-Rac). Similar effects were also observed in BCs expressing *rho1 RNAi* (29°C), *rok RNAi* (29°C), and *RacN17* (25°C), which supposedly affect either the Myosin II function or the actin polymerization function of the actomyosin network (Figure 4A, third row; quantified in Figures 4B and 4C). Together, our results show that Myosin II and the upstream Rho, Rok, and Rac that regulate Myosin II and F-actin's functions are essential for cell-cell communication during collective migration.

Inactivation of Myosin II by CALI Disrupts Cell-Cell Communication

In order to further demonstrate the role of actomyosin network in cell-cell communication, we next applied CALI to locally and directly inhibit Myosin II's function in individual BCs. We reasoned that, without the mechanical tension provided by a supracellular actomyosin network, BCs would lose effective cell-cell communication with each other. To disrupt such supracellular actomyosin network, we first used CALI (488 nm, 100% laser power) to inhibit Sqh-GFP at two cortical regions at the sides of BC cluster to break the cortical tension there. Next, we illuminated (458-nm laser at 8% power) at the rear of BC cluster to photoactivate exogenous Rac. Similar to the controls (with no CALI, or CALI of PH-GFP), new protrusions could

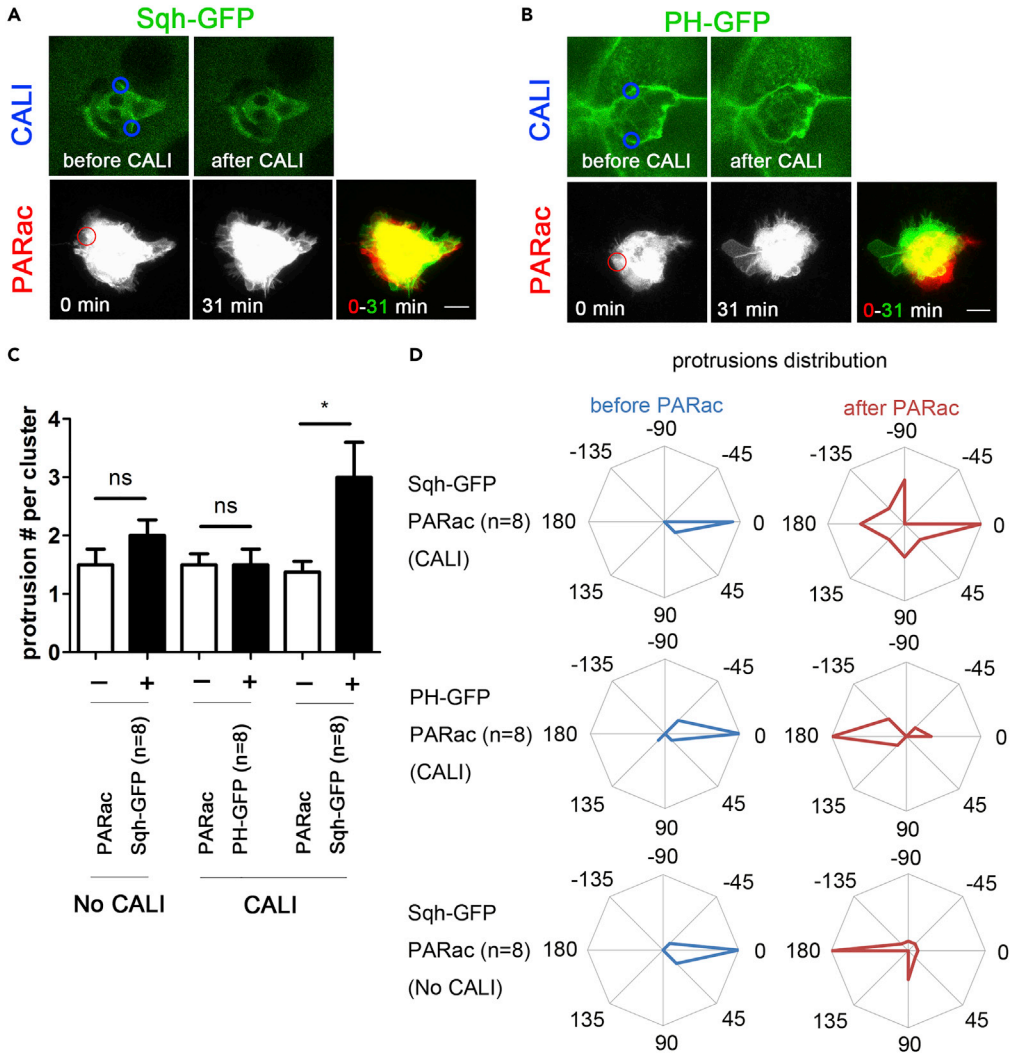

Figure 5. Local CALI of Sqh-GFP Impairs Cell-Cell Communication

(A) After applying CALI on Sqh-GFP-expressing BCs, local activation of PA-Rac in the rear region of BC cluster induced a new protrusion but failed to retract leading protrusion. Furthermore, several new protrusions were formed after CALI (net increase of protrusion number, as quantified in [C]), and they failed to retract after photoactivation of PA-Rac, demonstrating a loss of cell-cell communication. Blue circles indicate CALI positions and the red circles indicate photoactivation regions.

(B) After CALI on PH-GFP-expressing BCs (negative control), local activation of PA-Rac induced a new protrusion and retracted the leading protrusion in 31 min (no net increase of protrusion number, as quantified in [C]), demonstrating effective cell-cell communication.

(C) Quantification of average protrusion number per cluster. *, $p < 0.05$; ns, not significant (Student's t test); data are represented as mean ± SEM. n = 8 for all the three experiments.

(D) Analysis of protrusion distribution by the radar diagram. n = 8 for all three experiments. Scale bars: 10 μm.

be induced from the rear BCs. But contrary to the controls, the leading protrusions of BC clusters treated with CALI of Sqh-GFP failed to retract after 31 min. Furthermore, ectopic protrusions were extended all around BC clusters (Figure 5A; quantified in Figures 5C and 5D), indicating a disruption of cell-cell communication. In contrast, CALI of PH-GFP did not induce more ectopic protrusions in 31 min and the original leading protrusion retracted successfully after photo-activating Rac at the rear (Figure 5B; quantified in Figures 5C and 5D), indicating an effective cell-cell communication. Taken together, our results demonstrate that the supracellular actomyosin network and its associated mechanical tension likely mediates cell-cell communication in BC cluster.

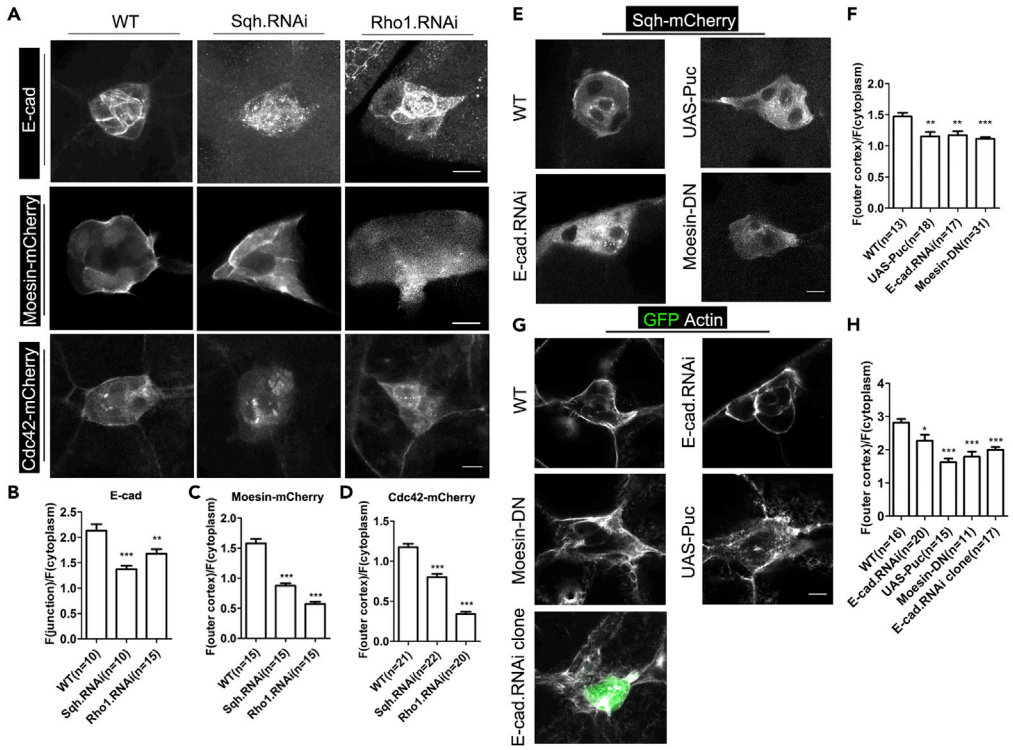

Figure 6. Inter-dependence between the Supracellular Actomyosin Network and Molecules Essential to Cell-Cell Communication

(A) Confocal images showing that loss of Rho1 or Sqh leads to disruption of the distribution of E-cadherin (E-cad, first row, quantified in [B]), Moesin-mCherry (second row, quantified in [C]), and Cdc42-mCherry (third row, quantified in [D]).

(B) The disruption of E-cad distribution is quantified as the reduced ratio between E-cad level at the apical junction (fluorescence intensity at the junction) and E-cad level in the cytoplasm (fluorescence intensity in cytoplasm).

(C and D) The disruption of Moesin or Cdc42 distribution is quantified as the reduced ratio between Moesin-mCherry or Cdc42-mCherry level (fluorescence intensity) at the outer cortex and its respective level (fluorescence intensity) in the cytoplasm.

(E and F) Confocal images showing that loss of E-cad or Moesin or overexpression of Puc leads to disruption of the distribution of Myosin II patches, which is quantified in (F) as the reduced ratio of Sqh-mCherry level (fluorescence intensity) at the outer cortex over its level (fluorescence intensity) in the cytoplasm.

(G and H) Loss of E-cad or Moesin or overexpression of Puc leads to disruption of F-actin distribution at the outer cortex (cluster periphery) and increased F-actin levels in the BC cytoplasm except for *E-cad RNAi*, which reduced F-actin level in both the outer cortex and cytoplasm. *E-cad RNAi clone* means only a clone of GFP-labeled BCs expresses the *E-cad RNAi*. The results are further quantified in (H) as the reduced ratio of the F-actin level at the outer cortex over F-actin level in the cytoplasm. Rhodamine phalloidin labels F-actin.

*, $p < 0.05$; **, $p < 0.01$; ***, $p < 0.001$ (Student's t test); data are represented as mean ± SEM. Scale bars: 10 μm.

Underlying Mechanisms of Cell-Cell Communication

Our study has shown that the supracellular actomyosin network provides an important physical means for cell-cell communication. Recent works had attempted to explore the molecular mechanism underlying cell-cell communication and found that it required E-cadherin, JNK pathway that promotes cell adhesion between BCs, Rab11, the cytoskeletal protein Moesin (trafficked by Rab11), and Cdc42 (required for Moesin activation [Colombie et al., 2017]) during collective migration of BCs. In light of this knowledge, it is conceivable that supracellular actomyosin network provides the critical missing link that physically connects all these components.

To test the above idea about the underlying mechanism of cell-cell communication, we then examined the distribution pattern of E-cadherin, Cdc42, and Moesin within the BC cluster while the supracellular actomyosin network was perturbed. We demonstrated that the distribution of E-cadherin, Cdc42, and Moesin was markedly disrupted when Myosin II function was reduced by *sqh RNAi* or *Rho RNAi* (Figures 6A–6D, S1D, and S1E). This

result confirms that perturbation of the actomyosin network leads to disruption of cell-cell communication, as manifested in the mislocalization of molecules critical for cell-cell communication including Moesin, Cdc42, and E-cadherin. Conversely, we disrupted cell-cell communication by downregulating E-cadherin, Moesin, and JNK signaling in the BCs and then determined their effects on the supracellular actomyosin network (Figures 6E–6H). Our data demonstrated that the organization of actomyosin network, as represented by the distribution pattern of Myosin II patches and cortical F-actin, was being significantly disrupted (Figures 6E–6H). This result further demonstrates the inter-dependence between the supracellular actomyosin network and molecules that are essential to cell-cell communication (E-cadherin, Moesin, Cdc42). Taken together, these results strengthen our conclusion that the supracellular actomyosin network mediates cell-cell communication between BCs, and they provide mechanistic details on how the supracellular structure composed of actomyosin, Moesin, Cdc42, and E-cadherin mediates cell-cell communication.

Disruption of Rho/Rok/Myosin II Pathway Leads to Ectopic Protrusions

The presence of a supracellular cortical actomyosin network that provides mechanical tension led us to hypothesize that it could also be the means to shape a front-polarized morphology of the BC cluster and inhibit the formation of ectopic protrusions. To test this idea, we attempted to disrupt the actomyosin network in BCs by reducing the function of individual members of Rho/Rok/Myosin II pathway. We found that numerous ectopic protrusions extended from BCs (Figures 1F, S6A, and S6B), similar to the results from the flip-out and CALI experiments (Figure 2). These ectopic protrusions were dynamic as revealed by live imaging (Figure S6C; and Video S7). Together with the flip-out and CALI results, these results further support the notion that the actomyosin network limits ectopic protrusion formation and is required for a polarized cluster morphology.

The Presence of Two Distinct Actin Populations in BCs

Myosin II and actin filaments (F-actin) are two major components of any actomyosin structure. We next examined the effects from reducing the activity of actin polymerization and thus the level of F-actin through the inhibition of the small GTPase Rac, which is the major actin polymerization promoter. Strong inhibition of Rac through expressing dominant negative form of Rac (*UAS-RacN17*) at 29°C resulted in severe block of BC migration, rounding of the BC cluster and complete loss of prominent protrusions, as consistent with previous reports (Figures S6D–S6F) (Geisbrecht and Montell, 2004; Zhang et al., 2011). Both the cortical actin (outside peripheral and inside junctional) and cytoplasmic actin levels were dramatically reduced (Figures S6D and S6G). It is known that expression of UAS-transgene by the Gal4 transcription factor is significantly higher at 29°C than at 25°C (Duffy, 2002). We found that moderate inhibition of Rac activity through expression of *UAS-RacN17* at 25°C caused much less severe migration defects (Figure S6E). Interestingly, these BC clusters are much more likely to extend non-leading or ectopic protrusions than the wild-type BCs (Figures S6D and S6F). Furthermore, we found that F-actin levels were significantly increased in the cytoplasmic region, whereas the F-actin level at the cortical region (outside peripheral) was significantly reduced (Figures S6D and S6G). The very different distribution patterns of F-actin (29°C versus 25°C) and the opposite phenotypes of over-abundance of protrusions (at 25°C) and absence of any protrusion (at 29°C) led us to propose that the strong or moderate Rac reduction each affects a different aspect or population of actin cytoskeleton. A previous study showed that there are two distinct F-actin networks in single non-tumorigenic rat liver epithelial cells (IAR-2 [Lomakin et al., 2015]). One network is associated with Myosin II and forms cortical actomyosin bundles, whereas the other actin network is involved in dendritic growth required for lamellipodial protrusions. Disruption of Myosin II activity and thus the first network resulted in overgrowth of the dendritic network and increased formation of protrusions (Lomakin et al., 2015). Our results suggest that BCs may also contain two distinct F-actin networks. First, reduction of Rac activity at 29°C and at 25°C both affected the cortical actin network that is associated with Myosin II. Indeed, significant reduction of Sqh-GFP and P-Myosin II at BC periphery accompanied reduction of cortical F-actin for RacN17 at 25°C (Figures S7A–S7E), indicating that the actomyosin network was disrupted by Rac loss of function. Second, strong loss of function of Rac (at 29°C) resulted in strong reduction in levels of cytoplasmic F-actin (Figures S6D and S6G), which supposedly includes the sub-membranous dendritic F-actin network. On the contrary, the second cytoplasmic network is not reduced by moderate Rac reduction (at 25°C) since cytoplasmic F-actin level and number of ectopic protrusions are not decreased but rather increased (Figures S6D, S6F, and S6G). Consistently, mild reduction of Rac by heterozygosity of *rac1*, *rac2*, and *mtl* mutations exhibited similar phenotypes of ectopic protrusions as well (Figure S6H). Together, these results implicate the presence of two distinct F-actin networks, which are affected to different degrees by either strong or moderate Rac loss of function.

To further demonstrate that these two distinct F-actin populations exist and function differently, we attempted to disrupt each actin network using genetic means and then observe the resulting molecular and morphological changes. Expressing *RNAi* of *rho1* or *sqh* in all BCs (driven by *slbo-Gal4*) is expected to disrupt the function of the first actin network, which is the cortical actomyosin network. In addition, Moesin was previously shown to localize at the periphery of BC clusters and was thought to link the actomyosin network to the cell membrane (Ramel et al., 2013). BC clusters expressing dominant negative form of Moesin (DN-Moesin) also displayed ectopic protrusions, similar to the loss-of-function phenotypes of *rho1* and *sqh* (Figure S6A). Furthermore, expression of DN-Moesin and *moesin RNAi* reduced the P-Myosin II staining in the cluster periphery, whereas *sqh RNAi* expression conversely decreased the peripheral localization of Moesin-mCherry, demonstrating the aforementioned interdependence of Moesin and actomyosin on the cluster periphery (Figures 6A, 6C, S7D, and S7E). Therefore, reducing Moesin's function is also expected to disrupt the integrity of the first actin network. Indeed, we found that overall F-actin level at the cortical region (adjacent to nurse cell membrane) was significantly reduced in *rho1 RNAi*, *sqh RNAi*, and DN-Moesin expressing BCs (Figures 6G, 6H, S6I, and S6J). Moreover, confocal images showed that the peripheral F-actin staining no longer appeared continuous (as in control) but appeared fragmented (Figures 6G, 6H, S6I, and S6J). Importantly, the overall levels of cytoplasmic F-actin, especially those close to the membrane region, are markedly increased. This result suggests that the disruption of the first (cortical) F-actin network leads to the upregulation of the second dendritic (cytoplasmic and sub-membranous) F-actin population. We think that there may be two likely explanations for this phenomenon. First, loss of physical and mechanical tension allows precocious and easy formation of protrusions under the membrane, where low level of polymerization of the sub-membranous dendritic actin network is normally not sufficient to power a large protrusion forward. Second, disruption of the first actin network results in excess of monomeric (G-) actin or short actin filaments, which could lead to the increased polymerization and growth of the second dendritic actin network. The first (physical) and second (chemical) scenarios may not be exclusive of each other but could exist simultaneously.

Furthermore, expression of *sqh* or *rho1 RNAi* resulted in appearance of ectopic regions of strong actin polymerization, as indirectly shown by the presence of active Rac (Figures S6K and S6L), which is measured by a previously reported Rac-FRET bio-sensor (Wang et al., 2010). In wild-type BC clusters, Rac-FRET displayed a significant asymmetry toward the front of clusters (Figures S6K and S6L). Reduction of Myosin II or Rho1 activity abrogated this asymmetry and resulted in ectopic (non-leading) regions of locally high Rac-FRET (Figures S6K and S6L). Indeed, high FRET signal could exist at single BCs at the rear or lateral side of clusters or simultaneously in multiple BCs.

Next, we attempted to specifically disrupt the second dendritic actin network and determine its effect on the first actin network and the BC behavior. Arp2/3 complex is known to be essential for the polymerization of the dendritic actin network and is regulated by the upstream Rac signaling and Scar/Wave complex (Disanza et al., 2005). Reducing the function of Arp2/3 complex is expected to affect the second (dendritic) F-actin network. We found that *RNAi* of *arp2* and *arp3* each resulted in loss of leading and non-leading protrusion as well as reduction of level of sub-membranous F-actin (Figures 7A and 7B), especially those close to the membrane of leading protrusion. Furthermore, the first actin network appeared unchanged since the level and distribution pattern of the cortical F-actin at the cluster periphery are similar to those of the control (Figures 7A and 7B). This result suggests that reduction of the second dendritic F-actin network does not significantly affect the cortical actomyosin network.

In addition to the genetic experiments, we attempted to utilize optogenetics to provide more evidence for interaction between the two distinct F-actin population. Upon CALI treatment of Sqh-GFP in a single BC (Figure S8), which would locally inhibit Myosin II's function and thus affect the integrity of the supracellular actomyosin network, F-actin levels in the peripheral membrane (outer cortex) region of all BCs were immediately (within seconds) and significantly reduced and the F-actin levels in cytoplasmic region of all BCs were immediately and significantly increased, resulting in an elevated cytoplasmic/outer cortex ratio as compared with those of No-CALI and PH-GFP CALI controls. This result supports our conclusion that the outer-cortical actomyosin network interacts with the cytoplasmic dendritic actin network and that the organization of the second dendritic actin network could be changed by perturbation in the first actomyosin network.

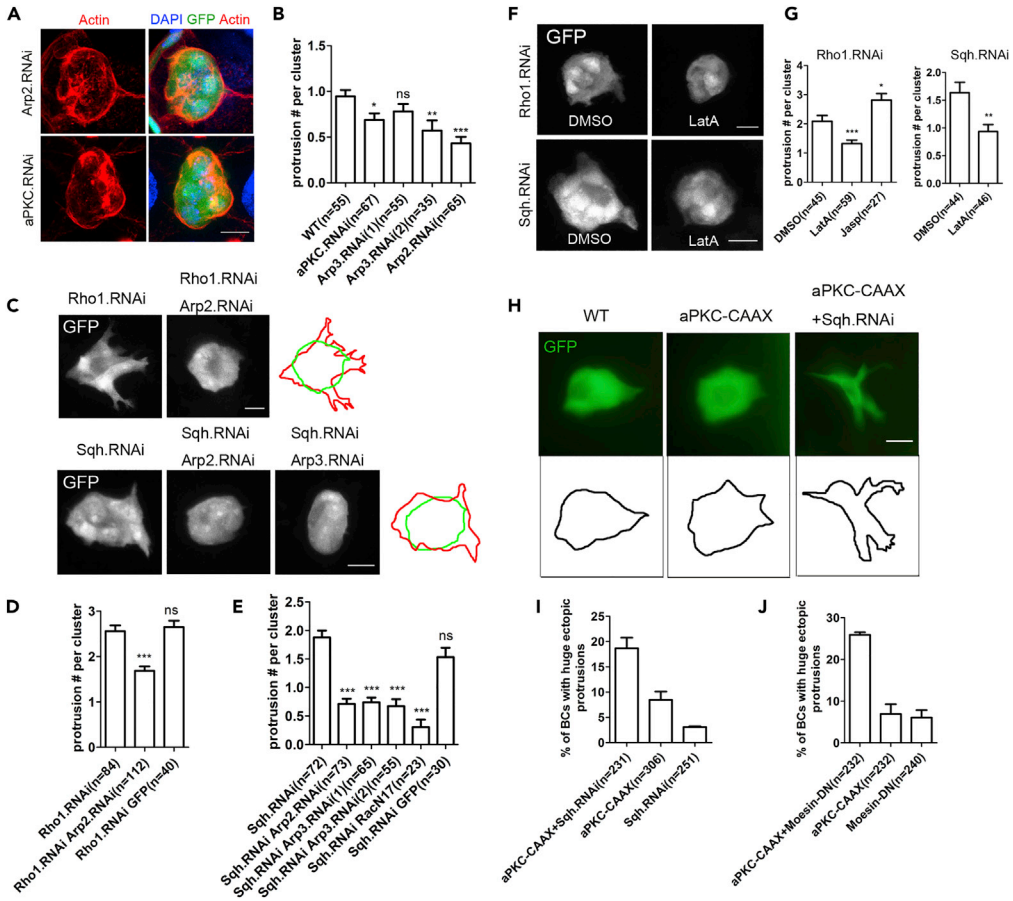

Figure 7. Balance between Peripheral and Cytoplasmic Actin Populations Shapes the Morphology of BC Cluster

(A) Confocal images showing that GFP-labeled BCs lose the leading protrusions and become more rounded as a result of expressing *arp2* and *aPKC RNAi* by the *slbo-Gal4* driver. Note that the distribution of peripheral or outer cortical F-actin is similar to that of wild-type clusters.

(B) Quantification of percentages of BC cluster without protrusions for the indicated genotypes. *arp3 RNAi(1)*, 35,260 (VDRC); *arp3 RNAi(2)*, 7558R-1 (NIG).

(C) Ectopic protrusions caused by loss of function of Rho1 or Sqh were rescued by expression of *arp2 RNAi* or *arp3 RNAi*.

(D and E) The rescues were quantified by the average number of protrusions per cluster for the indicated genotypes.

(F) LatA treatment rescued ectopic protrusions as caused by *rho1 RNAi* or *sqh RNAi*. DMSO was used as a control.

(G) Quantification of average number of protrusions after drug treatment.

(H) Representative fluorescent images showing that huge ectopic protrusions are formed when simultaneously expressing aPKC-CAAX and *sqh RNAi*.

(I and J) Quantification of BCs with huge ectopic protrusions for the indicated genotypes.

*, $p < 0.05$; **, $p < 0.01$; ***, $p < 0.001$; ns, not significant (Student's t test); data are represented as mean ± SEM. Scale bars: 10 μm. See also Figures S6–S8 and Video S7.

Interaction between Peripheral Actin and Cytoplasmic Actin Populations Shapes the Morphology of BC Cluster

Lastly, we attempted to determine how the interaction between the two distinct F-actin populations and their associated forces shape the BC morphology and behavior. It was previously shown that aPKC promoted protrusions and actin polymerization in BCs (Wang et al., 2018). We found that knockdown of aPKC achieved similar effects as those of *arp2* and *arp3 RNAi*, which are marked reduction of leading and non-leading protrusions, rounding of BC clusters, and no gross changes in the first actin network (Figures 7A and 7B). This result suggests that aPKC, like Arp2/3 complex, specifically affects the second dendritic population. Interestingly, the rounding of BC clusters implies that without the protrusive force from the leading protrusion the contractile force from the first actin network would be the dominant force, turning a spindle-shaped (polarized) wild-type BC cluster into a rounded BC cluster. If our assumption is

correct, the ectopic protrusions observed in *rho1 RNAi* or *sqh RNAi* (Figure S6A) is a combined result of the lack of constraining or contractile force from the first actin network and increased protrusive force as caused by increased polymerization of the second actin network in non-leading BCs. To test this idea, we removed Arp2 or Arp3 function in the background of *rho1 RNAi* or *sqh RNAi* and found that the phenotype of ectopic (non-leading) protrusions was remarkably rescued (Figures 7C–7E). This result indicates that the ectopic protrusions depend on the increased polymerization of the second dendritic actin population, which supposedly results in increased protrusive force. Consistently, reduction of level of actin polymerization by Latrunclin A (LatA) treatment and RacN17 (29°C) expression also resulted in reduction of ectopic protrusions (Figures 7E–7G). On the other hand, when we attempted to specifically over-activate the second actin network and increase its protrusive force by expressing activated aPKC (aPKC-CAAX) in the wild-type background, BCs only extended ectopic protrusions of moderate size (Figures 7H–7J). However, expression of aPKC-CAAX in the background of *sqh RNAi* or DN-Moesin expression, which reduced the integrity of the first actin network, resulted in BC clusters extending very large protrusions; this phenotype was far more severe than aPKC-CAAX, or *sqh RNAi*, or DN-Moesin alone (Figures 7H–7J). This result highlights the importance of the first actomyosin network in restraining the formation and extension of ectopic protrusion, as reducing the contractile force allows the protrusive force to become the dominant force and the eventual formation of very large protrusions. Taken together, our data reveal the antagonizing interaction between these two actin networks. The outward pushing or protrusive force as generated from Arp2/3-dependent actin polymerization and the inward restraining force as produced from actomyosin contraction together determine the morphology of BC cluster.

DISCUSSION

A previous study on collective migration of MDCK cells in a 2D environment *in vitro* demonstrated the presence of a pluricellular actomyosin cable along the edge of the migratory cell sheet or finger (Reffay et al., 2014). It was further shown that the actomyosin structure is tensile and its severance by laser ablation at non-leading positions could relieve the mechanical tension and induce formation of large ectopic protrusions. Therefore, it concludes that mechanical tension mediated by the pluricellular actomyosin cable prevents the initiation of new protrusions in cells at non-leading positions (Friedl et al., 2014; Reffay et al., 2014), hence maintaining the front polarized collective morphology. Here, we demonstrate that a supracellular actomyosin network encompasses the surface of the entire BC cluster. Different from the thin linear actomyosin cable along the leading finger of MDCK sheet, BC cluster possesses a distinct supracellular structure in which an elaborate actomyosin network is present throughout the entire surface of the BC cluster. The integrity of this actomyosin structure depends on Myosin II (Sqh), Rho1, Rok, Moesin, and Rac and is critical for the collective migration and polarized morphology of BCs in a 3D environment *in vivo*. We further show that the actomyosin network plays a confining or restricting role on initiation of new protrusions, since inhibition of Sqh activity and thus Myosin II's contractile ability by genetic means and CALI method loosens the confinement, resulting in formation of ectopic protrusions at the side and rear BCs. Unlike the more stable linear actomyosin cable of MDCK sheet, the actomyosin network on the peripheral surface of BC cluster is highly dynamic. Live imaging reveals a dynamic organization of Myosin II patches (large aggregates) and spots (small aggregates) on the surface of BCs, with the size and number of patches negatively correlating with the size of leading protrusion. Globally, an overall increase in the patches and decrease in the spots in the entire actinomyosin network seems to correlate with protrusion retraction, whereas a decrease in patches and increase in spots correlates with protrusion extension. Locally, movement or flow of Myosin II patches along the length (toward the tip) of leading protrusion correlates with the retraction of protrusions. However, the precise underlying mechanism of how different Myosin II organizations exert their corresponding morphological changes remain to be further determined.

Interestingly, we find that another important function of the actomyosin network is to mediate cell-cell communication between BCs. Previous works have demonstrated that E-cadherin and JNK signaling, which promote cell adhesion between BCs, are required for cell-cell communication, using the same PA-Rac activation method (Cai et al., 2014; Wang et al., 2010). Furthermore, Rab11, Moesin (supposedly trafficked by Rab11), and Cdc42 (required for Moesin activation) were also shown to be required (Ramel et al., 2013). Here, we provide direct evidence that the supracellular actomyosin network functions to mediate cell-cell communication by means of mechanical tension, as demonstrated by the Sqh-GFP's CALI experiment. Furthermore, we show that the integrity of supracellular actomyosin depends on Moesin, JNK, and E-cadherin. Conversely, the correct localization of Moesin, Cdc42, and E-cadherin also depends on Myosin II activity. Together, these findings provide mechanistic details that supracellular actomyosin

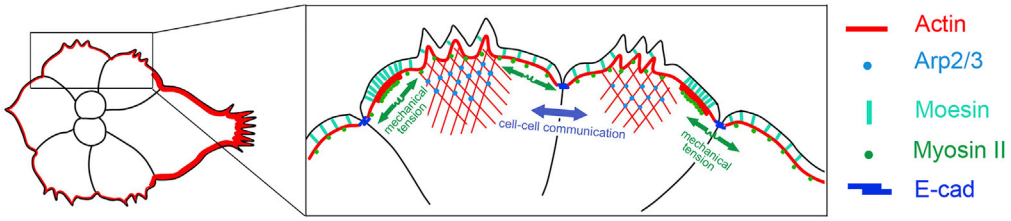

Figure 8. Schematic Diagram of the Proposed Model

The supracellular actomyosin network mediates cell-cell communication and shapes collective morphology of BCs. Cortical tension as produced by the actomyosin network mediates cell-cell communication and prevents formation of ectopic protrusions. Mechanistic details are explained in Discussion.

could be attached to the peripheral plasma membrane via Moesin and anchored to the adherens junctions (AJs) of adjacent BCs via E-cadherin. The mechanical force that is mediated by the contractile supracellular structure (e.g., through actomyosin-AJ-actomyosin-AJ …) could serve as the physical means of cell-cell communication (Figure 8). It is conceivable that, as the front cell extends a large protrusion, a significant increase of mechanical tension will be felt by other BCs at the side or rear position, resulting in suppression of protrusion formation in those BCs. On the other hand, if a large protrusion is induced in the rear BC (by photo-activation of Rac), the resulting increase of tension would be transmitted to BCs at the side and front positions, leading to suppression of minor protrusion at the side and retraction of large protrusion at the front.

Lastly, our study also reveals the presence of two distinct F-actin pools that regulate the protrusion formation and cluster morphology (Figure 8). The actomyosin network on the periphery of BC cluster represents the first F-actin pool, and the level and distribution of this pool could be affected by the Rho/Rok/Myosin II pathway, Moesin, and Rac. The second pool is localized close to the sub-membranous region of the cytoplasm and represents the dendritic F-actin population that depends on Arp2/3, Rac, and aPKC. We find that disruption of the first pool increases the F-actin level of the second pool, suggesting an antagonizing interaction between the two pools and that actin monomers or short filaments released from the disruption of stable actomyosin network feeds into the dynamic growth of the dendritic F-actin network. Our results are consistent with a previous report by Lomakin and coworkers, which similarly demonstrated two distinct F-actin pools in the cultured epithelial cell line IAR-2 (Lomakin et al., 2015). Interestingly, they found that the cortical actomyosin cable is present in static individual IAR-2 cells with non-polarized morphology, whereas inhibition of Myosin II's regulatory light chain switches those cells to migratory morphology (with front-rear polarity) that is accompanied by the presence of Arp2/3-dependent dendritic F-actin network. Moreover, disruption of the cortical actomyosin cable leads to elevation of G-actin level and increased polymerization of dendritic actin near the membrane of lamellipodial protrusions. Results from their study support the model that both F-actin populations compete for the same G-actin pool and hence antagonize each other. Furthermore, their model suggests that these two distinct F-actin pools could not both dominate in the same cell state; either the actomyosin pool dominates in the non-polarized (epithelial-like) cells or the dendritic pool dominates in the front-polarized migratory (mesenchymal) cells. Interestingly, our results show that both pools appear to be present in high levels in the BCs. This coexistence of and balance between the two F-actin pools could be a unique feature of collectively migrating cells, which need to possess both epithelial integrity that is needed for cell-cell communication within the collective group and migratory polarization that is characteristic of mesenchymal cells.

Limitations of the Study

In this study, we reveal the presence of a supracellular actomyosin network, which functions to mediate cell-cell communication between BCs. However, the underlying cell-cell communication mechanism needs to further elucidated. We provide genetic evidence that demonstrated interdependence between actomyosin network and molecules that were previously shown to be essential for cell-cell communication, including E-cadherin, Moesin, and Cdc42 (Figure 6). However, faster and higher-resolution live-imaging will be needed to reveal how the actomyosin network physically interacts with each of these molecules *in vivo* and in real time. Owing to the limits in speed and resolution of our confocal microscopes and the small size and internal position of the BC cluster, these experiments are currently technically challenging to carry out. Results from these proposed experiments could provide mechanistic details on how molecular

changes in organization of actomyosin network and those essential molecules together effect morphological changes in BC behavior, such as extension and retraction of protrusions.

Resource Availability

Lead Contact

Further information and requests for reagents should be directed to and will be fulfilled by the Lead Contact, Jiong Chen (chenjiong@nju.edu.cn).

Materials Availability

This study did not generate new unique reagents.

Data and Code Availability

The published article includes all datasets generated or analyzed during this study.

METHODS

All methods can be found in the accompanying Transparent Methods supplemental file.

SUPPLEMENTAL INFORMATION

Supplemental Information can be found online at https://doi.org/10.1016/j.isci.2020.101204.

ACKNOWLEDGMENTS

We are grateful to Dr. Cheng-yu Lee, Dr. Lei Xue, and Dr. Yang Hong, the Bloomington Drosophila Stock Center, Tsinghua University RNAi Stock Center, National Institute of Genetics Stock Center (Japan), and Vienna Drosophila RNAi Center for fly stocks. We thank A. Wodarz for Baz antibody. This work is supported by grants from the National Natural Science Foundation of China (31970743, 31571435) and Natural Science Foundation of Jiangsu Province (BK20171337) to J.C. and grants from the National Natural Science Foundation of China (31900563) and Natural Science Foundation of Jiangsu Province (BK20190303) to H.W.

AUTHOR CONTRIBUTIONS

Conceptualization, H.W., X.G., J.C.; Methodology, H.W., J.C., Xianping Wang, Xiaobo Wang; Formal analysis, H.W.; Investigation, H.W.; Writing – original draft, H.W., J.C.; Writing – review & editing, H.W., J.C., Xiaobo Wang; Visualization, H.W., J.C.; Supervision, J.C.; Project administration, H.W., J.C.; Funding acquisition, J.C., H.W.

DECLARATION OF INTERESTS

The authors declare no competing interests.

Received: February 1, 2019
Revised: March 23, 2020
Accepted: May 26, 2020
Published: June 26, 2020

REFERENCES

Aranjuez, G., Burtscher, A., Sawant, K., Majumder, P., and McDonald, J.A. (2016). Dynamic myosin activation promotes collective morphology and migration by locally balancing oppositional forces from surrounding tissue. Mol. Biol. Cell *27*, 1898–1910.

Britton, J.S., Lockwood, W.K., Li, L., Cohen, S.M., and Edgar, B.A. (2002). Drosophila's insulin/PI3-kinase pathway coordinates cellular metabolism with nutritional conditions. Dev. Cell *2*, 239–249.

Cai, D., Chen, S.C., Prasad, M., He, L., Wang, X., Choesmel-Cadamuro, V., Sawyer, J.K., Danuser, G., and Montell, D.J. (2014). Mechanical feedback through E-cadherin promotes direction sensing during collective cell migration. Cell *157*, 1146–1159.

Colombie, N., Choesmel-Cadamuro, V., Series, J., Emery, G., Wang, X., and Ramel, D. (2017). Non-autonomous role of Cdc42 in cell-cell communication during collective migration. Dev. Biol. *423*, 12–18.

Combedazou, A., Choesmel-Cadamuro, V., Gay, G., Liu, J., Dupre, L., Ramel, D., and Wang, X. (2017). Myosin II governs collective cell migration behaviour downstream of guidance receptor signalling. J. Cell Sci. *130*, 97–103.

del Valle Rodriguez, A., Didiano, D., and Desplan, C. (2011). Power tools for gene expression and clonal analysis in Drosophila. Nat. Methods *9*, 47–55.

Devreotes, P., and Janetopoulos, C. (2003). Eukaryotic chemotaxis: distinctions between directional sensing and polarization. J. Biol. Chem. *278*, 20445–20448.

Disanza, A., Steffen, A., Hertzog, M., Frittoli, E., Rottner, K., and Scita, G. (2005). Actin polymerization machinery: the finish line of signaling networks, the starting point of cellular movement. Cell Mol. Life Sci. *62*, 955–970.

Duffy, J.B. (2002). GAL4 system in Drosophila: a fly geneticist's Swiss army knife. Genesis *34*, 1–15.

Etienne-Manneville, S. (2014). Neighborly relations during collective migration. Curr. Opin. Cell Biol. *30*, 51–59.

Friedl, P., and Gilmour, D. (2009). Collective cell migration in morphogenesis, regeneration and cancer. Nat. Rev. Mol. Cell Biol. *10*, 445–457.

Friedl, P., Wolf, K., and Zegers, M.M. (2014). Rho-directed forces in collective migration. Nat. Cell Biol. *16*, 208–210.

Geisbrecht, E.R., and Montell, D.J. (2004). A role for Drosophila IAP1-mediated caspase inhibition in Rac-dependent cell migration. Cell *118*, 111–125.

Jacobson, K., Rajfur, Z., Vitriol, E., and Hahn, K. (2008). Chromophore-assisted laser inactivation in cell biology. Trends Cell Biol. *18*, 443–450.

Lomakin, A.J., Lee, K.C., Han, S.J., Bui, D.A., Davidson, M., Mogilner, A., and Danuser, G. (2015). Competition for actin between two distinct F-actin networks defines a bistable switch for cell polarization. Nat. Cell Biol. *17*, 1435–1445.

Lucas, E.P., Khanal, I., Gaspar, P., Fletcher, G.C., Polesello, C., Tapon, N., and Thompson, B.J. (2013). The Hippo pathway polarizes the actin cytoskeleton during collective migration of Drosophila border cells. J. Cell Biol. *201*, 875–885.

Majumder, P., Aranjuez, G., Amick, J., and McDonald, J.A. (2012). Par-1 controls myosin-II activity through myosin phosphatase to regulate border cell migration. Curr. Biol. *22*, 363–372.

Martin, A.C., Kaschube, M., and Wieschaus, E.F. (2009). Pulsed contractions of an actin-myosin network drive apical constriction. Nature *457*, 495–499.

Mayor, R., and Etienne-Manneville, S. (2016). The front and rear of collective cell migration. Nat. Rev. Mol. Cell Biol. *17*, 97–109.

Monier, B., Pelissier-Monier, A., Brand, A.H., and Sanson, B. (2010). An actomyosin-based barrier inhibits cell mixing at compartmental boundaries in Drosophila embryos. Nat. Cell Biol. *12*, 60–69.

Montell, D.J., Yoon, W.H., and Starz-Gaiano, M. (2012). Group choreography: mechanisms orchestrating the collective movement of border cells. Nat. Rev. Mol. Cell. Biol. *13*, 631–645.

Ou, G., Stuurman, N., D'Ambrosio, M., and Vale, R.D. (2010). Polarized myosin produces unequal-size daughters during asymmetric cell division. Science *330*, 677–680.

Pickering, K., Alves-Silva, J., Goberdhan, D., and Millard, T.H. (2013). Par3/Bazooka and phosphoinositides regulate actin protrusion formation during Drosophila dorsal closure and wound healing. Development *140*, 800–809.

Poukkula, M., Cliffe, A., Changede, R., and Rorth, P. (2011). Cell behaviors regulated by guidance cues in collective migration of border cells. J. Cell Biol. *192*, 513–524.

Qin, X., Hannezo, E., Mangeat, T., Liu, C., Majumder, P., Liu, J., Choesmel-Cadamuro, V., McDonald, J.A., Liu, Y., Yi, B., et al. (2018). A biochemical network controlling basal myosin oscillation. Nat. Commun. *9*, 1210.

Qin, X., Park, B.O., Liu, J., Chen, B., Choesmel-Cadamuro, V., Belguise, K., Heo, W.D., and Wang, X. (2017). Cell-matrix adhesion and cell-cell adhesion differentially control basal myosin oscillation and Drosophila egg chamber elongation. Nat. Commun. *8*, 14708.

Ramel, D., Wang, X., Laflamme, C., Montell, D.J., and Emery, G. (2013). Rab11 regulates cell-cell communication during collective cell movements. Nat. Cell Biol. *15*, 317–324.

Reffay, M., Parrini, M.C., Cochet-Escartin, O., Ladoux, B., Buguin, A., Coscoy, S., Amblard, F., Camonis, J., and Silberzan, P. (2014). Interplay of RhoA and mechanical forces in collective cell migration driven by leader cells. Nat. Cell Biol. *16*, 217–223.

Riedl, J., Crevenna, A.H., Kessenbrock, K., Yu, J.H., Neukirchen, D., Bista, M., Bradke, F., Jenne, D., Holak, T.A., Werb, Z., et al. (2008). Lifeact: a versatile marker to visualize F-actin. Nat. Methods *5*, 605–607.

Royou, A., Field, C., Sisson, J.C., Sullivan, W., and Karess, R. (2004). Reassessing the role and dynamics of nonmuscle myosin II during furrow formation in early Drosophila embryos. Mol. Biol. Cell *15*, 838–850.

Sano, Y., Watanabe, W., and Matsunaga, S. (2014). Chromophore-assisted laser inactivation–towards a spatiotemporal-functional analysis of proteins, and the ablation of chromatin, organelle and cell function. J. Cell Sci. *127*, 1621–1629.

Veeman, M.T., and McDonald, J.A. (2016). Dynamics of cell polarity in tissue morphogenesis: a comparative view from Drosophila and Ciona. F1000Res. *5*, https://doi.org/10.12688/f1000research.8011.1.

Wang, H., Qiu, Z., Xu, Z., Chen, S.J., Luo, J., Wang, X., and Chen, J. (2018). aPKC is a key polarity molecule coordinating the function of three distinct cell polarities during collective migration. Development *145*, dev158444.

Wang, X., He, L., Wu, Y.I., Hahn, K.M., and Montell, D.J. (2010). Light-mediated activation reveals a key role for Rac in collective guidance of cell movement in vivo. Nat. Cell Biol. *12*, 591–597.

Zhang, L., Luo, J., Wan, P., Wu, J., Laski, F., and Chen, J. (2011). Regulation of cofilin phosphorylation and asymmetry in collective cell migration during morphogenesis. Development *138*, 455–464.

iScience, Volume *23*

Supplemental Information

Supracellular Actomyosin Mediates Cell-Cell Communication and Shapes Collective Migratory Morphology

Heng Wang, Xuan Guo, Xianping Wang, Xiaobo Wang, and Jiong Chen

Supplemental Information

Supplemental figures

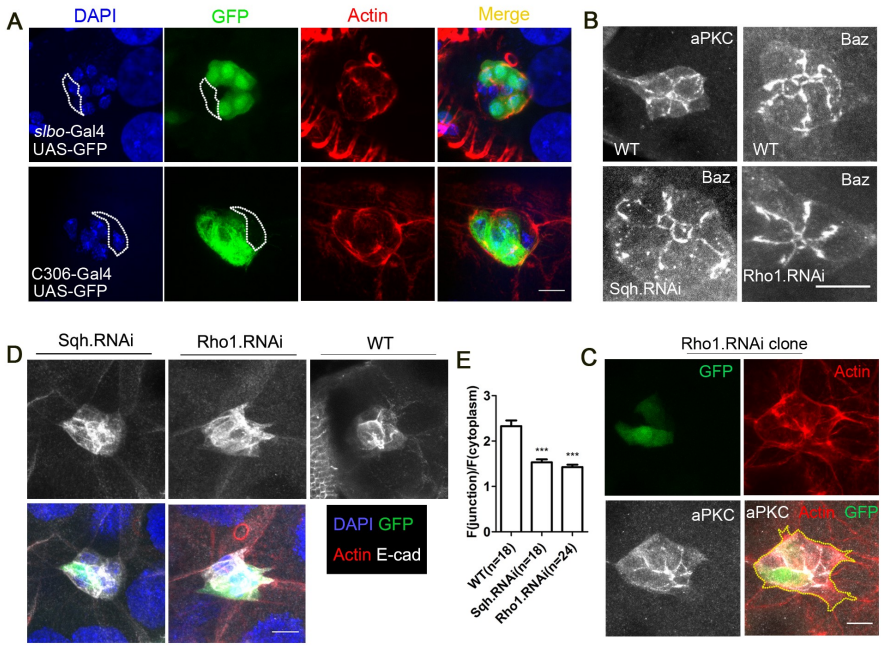

Figure S1. Non-uniform Gal4 expression from *slbo-Gal4* and *C306-Gal4* and distribution of polarity molecules by *sqh RNAi* or *rho1 RNAi*, Related to Figure 1 and Figure 2. (**A**) Confocal images showing rare mosaic expression of GFP from *slbo-Gal4* (first row) and *c306-Gal4* drivers (second row). Dashed lines indicated BCs without GFP expression. (**B**) Confocal images showing normal aPKC and Baz patterns in wild type BCs. Expressing *sqh RNAi* or *rho1 RNAi* by *slbo-Gal4* doesn't affect Baz. (**C**) Although ectopic protrusions are formed, aPKC pattern is not affected in *rho1 RNAi* expressing BC cluster that contains GFP-labeled single cell clone. Dashed lines highlight the outline of BC cluster. (**D**) The E-cadherin (E-cad) pattern is disrupted in mosaic BC clusters containing *sqh RNAi* or *rho1 RNAi* expressing clones that are labeled by GFP. (**E**) The disruption is quantified as the reduced ratio of E-cad level (Fluorescence intensity) at the junctions over the E-cad level (Fluorescence intensity) in the cytoplasm. ***, P<0.001; ns, not significant (Student's t-test); Data are represented as mean ± SEM. Scale bars: 10 μm.

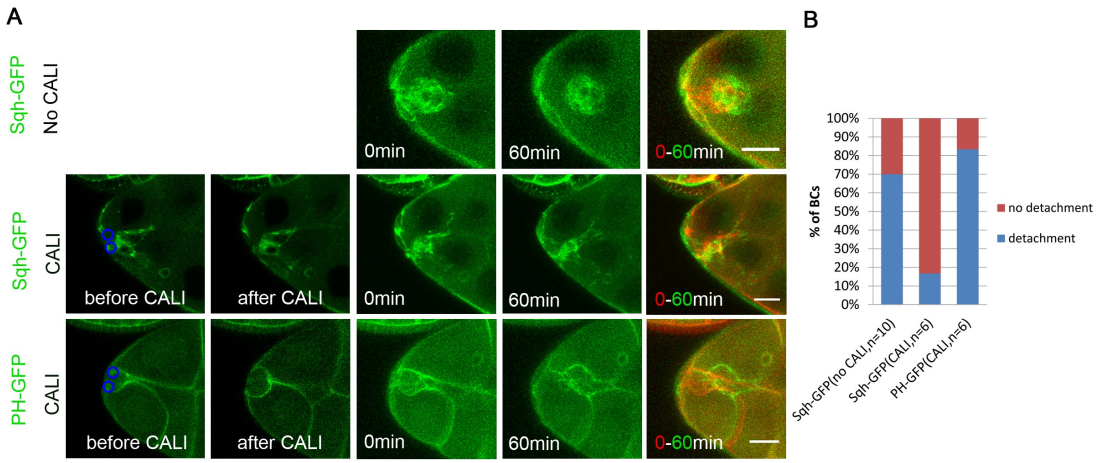

Figure S2. CALI of Sqh-GFP at the rear of BC cluster inhibits its detachment, Related to Figure 2. (**A**) Confocal images in the top row panels show that the Sqh-GFP expressing BCs without CALI treatment detaches from the follicle epithelium in 60 min. Panels in the second row show that CALI treatment at the rear of BC cluster causes its failure of detachment from the anterior tip of egg chamber in 60 min. The third row shows that CALI of PH-GFP as control does not affect BC detachment. Blue circles indicate regions of illumination. (**B**) Quantification of detachment of BC clusters for the indicated conditions. Scale bar: 20 μm.

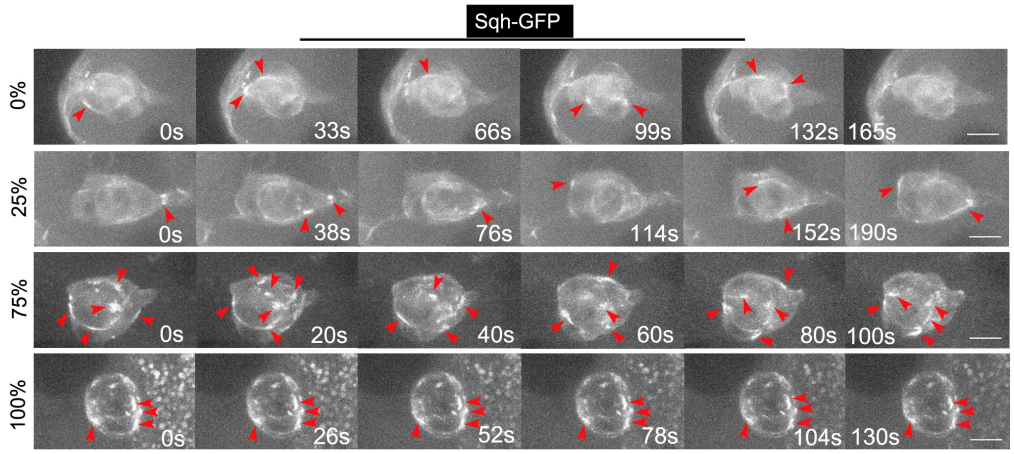

Figure S3. The dynamics of Myosin II patches on the surface of BC cluster, Related to Figure 3. Still images from time-lapse movies showing the dynamic movement of Myosin II patches (labeled with Sqh-GFP) on the surface of BC cluster at four different time points of migration. The percentages point to the migratory positions and thus reflects their corresponding migratory time points. 0% refers to BC cluster leaving the 0% position, indicating that BCs are at the phase of initiating their migration. 25% refers to BC cluster reaching the 25% position, meaning that BCs are at their early migratory phase. 75% refers to BC cluster reaching the 75% position, indicating the late migratory phase. Lastly, 100% refers to BC reaching the border, indicating the end of migration. Arrow heads indicate Myosin II patches. Scale bars:

10 μm.

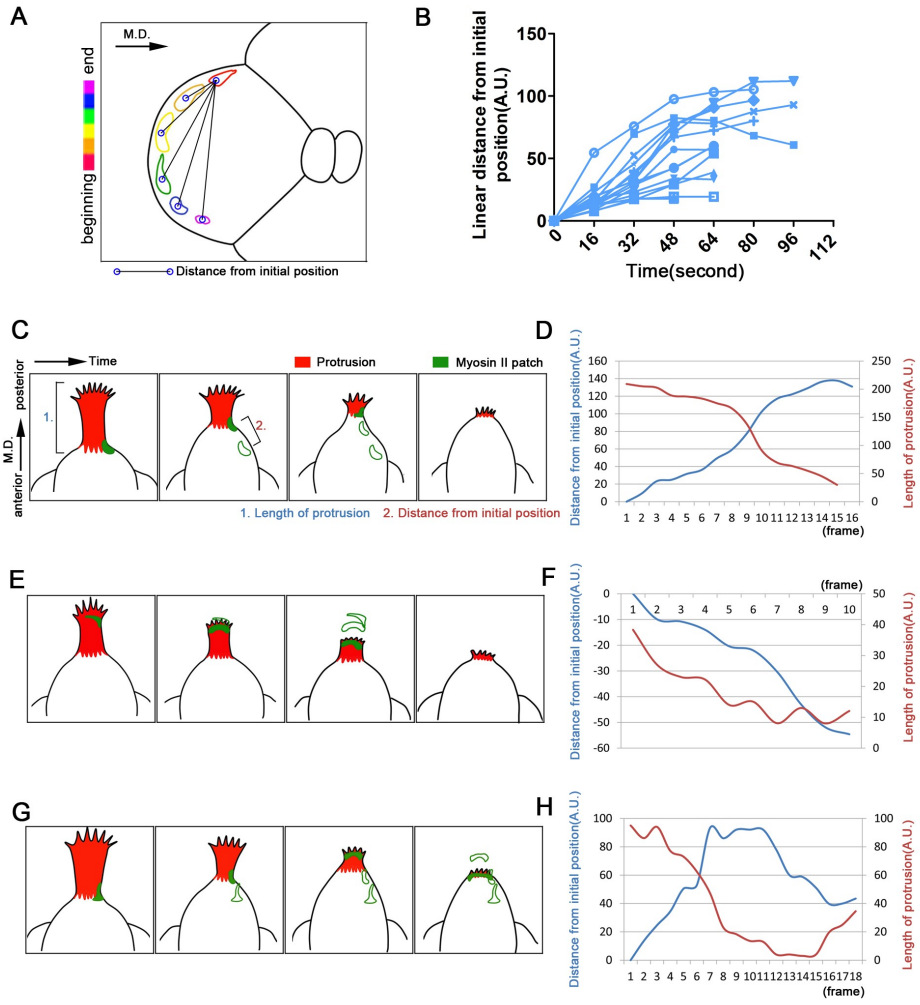

Figure S4. Distinct types of movement of Myosin II patches on BC's peripheral surface, Related to Figure 3. (**A**) Schematic diagram showing the motion trail of Myosin II patches along the surface of BC cluster (at the non-leading position). The multi-color circles represent the Myosin II patch at different time points. Red indicates the beginning or initial position. M.D. and arrow indicate migratory direction. Linear distances between Myosin II patches at the beginning and at other time points were measured as shown in (**A**), and the results were quantified in (**B**) to indicate the movement of Myosin II patches. The ever-increasing linear distances as the time progresses would indicate that the Myosin II patches move along the outer cell cortex in one direction only (i.e. not bi-directional). (**B**) The graph indicates that the Myosin II patches flow away from their initial position uni-directionally (n=16). Note that there is one sample with filled-square data points that display a moderate decrease in linear distances (from 48 seconds to 96 seconds). This is due to the large curvature of cell cortex of the sample BC and not due to the bi-directional flow (i.e. backward flow). (**C-H**) Three distinct types of flow of Myosin II patches at the leading protrusion are illustrated. (**C, D**) First, Myosin II patch forms at the basal

region of protrusion and moves towards the protrusion tip or the posterior until its disappearance near the tip of protrusion (10 out of 18). This flow accompanies a simultaneous retraction of leading protrusion, which is quantified and showed in (**D**) by one representative sample. The time interval between two consecutive frames is 15 seconds. (**E, F**) Second, Myosin II patch forms near the tip of protrusion and moves towards the base as protrusion shortens (3 out of 18). The correlation between movement of Myosin II patch and length of protrusion is quantified and showed in (**F**) by one representative sample. The time interval between two consecutive frames is 27 seconds. (**G, H**) Third, Myosin II patch forms at the base of protrusion and moves towards posterior to the tip of protrusion, then turns back toward anterior while the protrusion retracts (5 out of 18). This correlation between movement of Myosin II patch and length of protrusion is quantified and shown in (**H**) by one representative sample. The time interval between two consecutive frames is 27 seconds. M.D. and black arrow indicate migratory direction. Patches with filled green area indicate the current Myosin II patches, while the hollow patches with green outline indicate Myosin II patches at previous time points (**C, E, G**). The value of distance from initial position would be negative if Myosin II patches at later time points are located anterior to their initial positions (**F**).

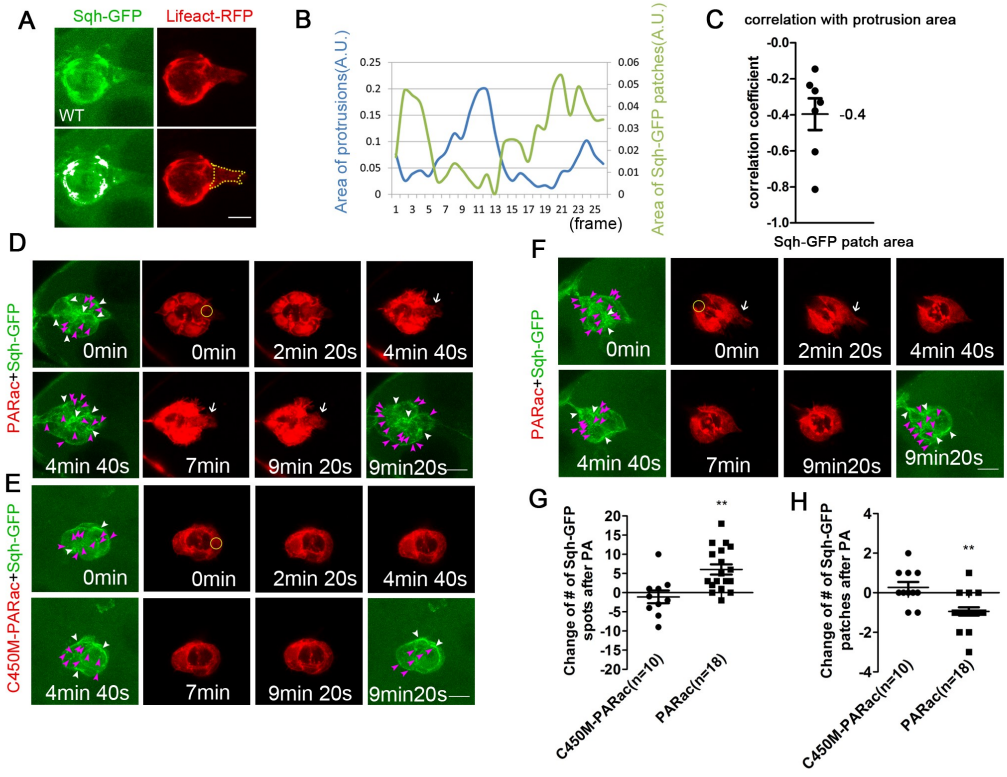

Figure S5. The relationship between Myosin II patches and protrusions in BC cluster, Related to Figure 3. (**A**) Confocal images showing the Myosin II patches (labeled with Sqh-GFP, green) and F-actin (labeled with Lifeact-RFP, red) in the wild type BCs. The area saturated with white signals in the second row are measured and

quantified as the area of Myosin II patches. The yellow dashed line outlines the region of protrusions to be measured. (**B**) Quantification of the dynamics of Myosin II patches and protrusions area over a period of time in one representative BC cluster. The time interval between two consecutive frames is 2 minutes. (**C**) Diagram showing that the area or size of Myosin II patches negatively correlate with protrusion size. Data points represent correlation coefficients (r-values) for individual BC clusters and -0.4 indicates the mean (n=7 clusters). (**D-F**) Images showing that increase of protrusion size through photoactivation of Rac results in decreased number of Myosin II patches but increase of Myosin II spots (**D**). This phenomenon was not observed in control (**E**). On the contrary, retraction of leading protrusion by Rac photoactivation in the rear side resulted in decreased number of Myosin II spots but more Myosin II patches (**F**). White arrowheads indicate Myosin II patches, purple arrowheads indicate Myosin II spots. White arrows mark leading protrusions. Yellow circles indicate regions of photoactivation. (**G, H**) Quantification showing the changes in the numbers of Myosin II spots (**G**) and patches (**H**) after photoactivation, i.e. the # of spots or patches after photoactivation minus the # of spots or patches before photoactivation. **, $P<0.01$; ***, $P<0.001$ (Student's t-test); Data are represented as mean ± SEM. Scale bars: 10 μm.

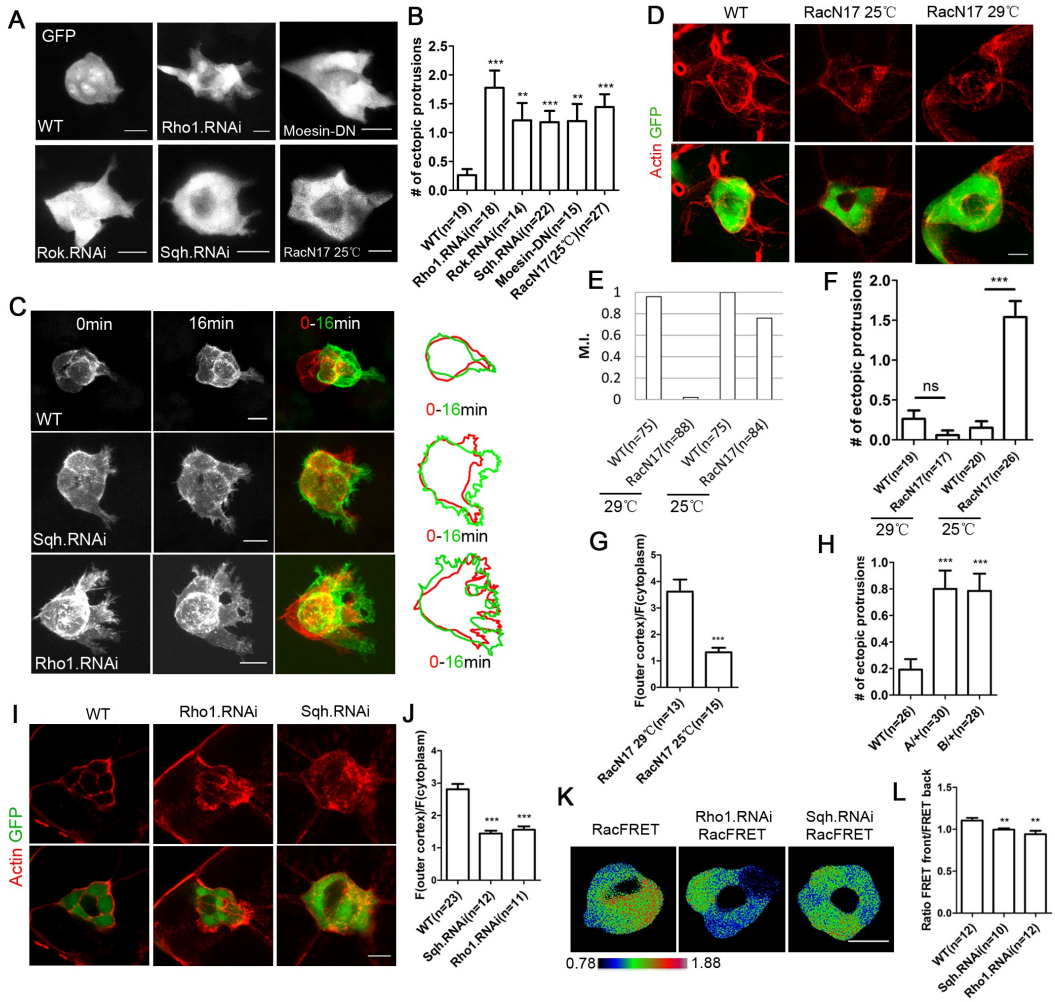

Figure S6. Loss of function of Rho1, Rok and Sqh leads to ectopic protrusions and RacN17 expression at 25°C and 29°C causes different effects on F-actin level and distribution, Related to Figure 7. (**A**) Confocal images of BC clusters labeled with GFP show ectopic protrusions in *rho1 RNAi*, *rok RNAi*, *sqh RNAi*, Moesin-DN, and RacN17 expressing BCs. (**B**) The average number of ectopic or non-leading protrusions per BC cluster for each genotype is measured and quantified. (**C**) Confocal images from live imaging using Lifeact-GFP (labeling F-actin) confirmed the phenotypes of ectopic protrusions and that these protrusions were dynamic. Schematic representations of the images are shown on the right, red and green diagrams correspond to the outlines of clusters at 0 min and 16 min respectively. (**D**) Confocal images indicate that ectopic protrusions are formed in BCs expressing RacN17 at 25°C. Moreover, F-actin distribution at the cluster periphery as observed in the WT BCs is disrupted, and increased levels of cytoplasmic F-actin are shown when compared to WT. BCs expressing RacN17 at 29°C display reduced levels of both peripheral F-actin and cytoplasmic F-actin, with the clusters appearing rounded. Actin filaments are labeled by Rhodamine-phalloidin and the *slbo-Gal4* driver is used for the experiments. (**E**) Migration index (M.I.) of BCs of different genotypes. See Transparent Methods for calculation of M.I. (**F**) Quantification of the average number of ectopic protrusions per BC cluster for each genotype. (**G**) Ratios of F-actin levels

in the outer cortex versus their levels in the cytoplasm. **(H)** Heterozygosity of *rac1, rac2*, *mtl* mutations induced ectopic protrusions. A/+ indicates the genotype of $rac1^{J11}rac2^{\triangle}mtl^{\triangle}$/+, and B/+ indicates the genotype of $rac1^{J10}rac2^{\triangle}mtl^{\triangle}$/+. **(I, J)** Loss of function of Rho1 or Sqh led to disruption of F-actin distribution at outer cortex (cluster periphery) and increased F-actin levels in the BC cytoplasm, which were quantified in (**J**) as the ratios between the F-actin levels (represented by the fluorescence intensity of Rhodamine Phalloidin) at the outer cortex and F-actin levels in the cytoplasm. (**K**) Representative Rac-FRET patterns in WT control and *rho1 RNAi* or *sqh RNAi* expressing BCs during their early stage of migration. Note that more FRET signals are localized in the front half of control BC cluster (left panel) and that Rac-FRET reporter is not expressed in the polar cells that are in the center of all BC clusters (all panels). (**L**) Quantification of the ratio of the Rac-FRET indices between the front and rear regions of each cluster for the indicated conditions. **, P<0.01; ***, P<0.001 (Student's t-test); Data are represented as mean ± SEM. Scale bars: 10 μm.

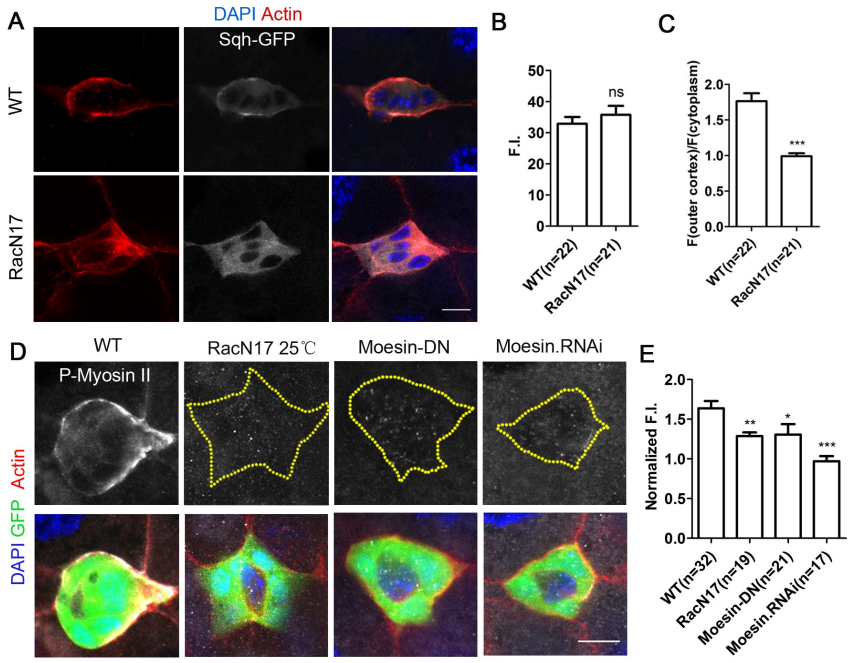

Figure S7. Loss of function of Rac and Moesin result in disruption of Myosin II distribution in BCs' outer cortex, Related to Figure 7. **(A)** Confocal images demonstrate that Sqh-GFP and F-actin (phalloidin) redistribute from outer periphery of BCs in WT (first row) to cytoplasm of BCs after expression of RacN17 at 25℃ (second row). Such redistribution is quantified in (**B, C**). **(B)** Quantification of total fluorescence intensity (F.I.) of Sqh-GFP in the BC clusters. **(C)** Quantification of the ratio of Sqh-GFP intensity between outer cortex and cytoplasm for the indicated genotypes. (**D**) Confocal images showing that P-Myosin II decreases at the periphery of BC cluster after expressing RacN17, Moesin-DN (the dominant negative form of Moesin) and *moesin RNAi*. Yellow dashed lines highlight the outline of border cells.

(**E**) Quantification of normalized fluorescent intensity of P-Myosin II in BCs of indicated genotypes. Fluorescent intensity of P-Myosin II in the nurse cells (NCs) is used for normalization. *, <0.05; **, P<0.01; ***, P<0.001 (Student's t-test); Data are represented as mean ± SEM. Scale bars: 10 μm.

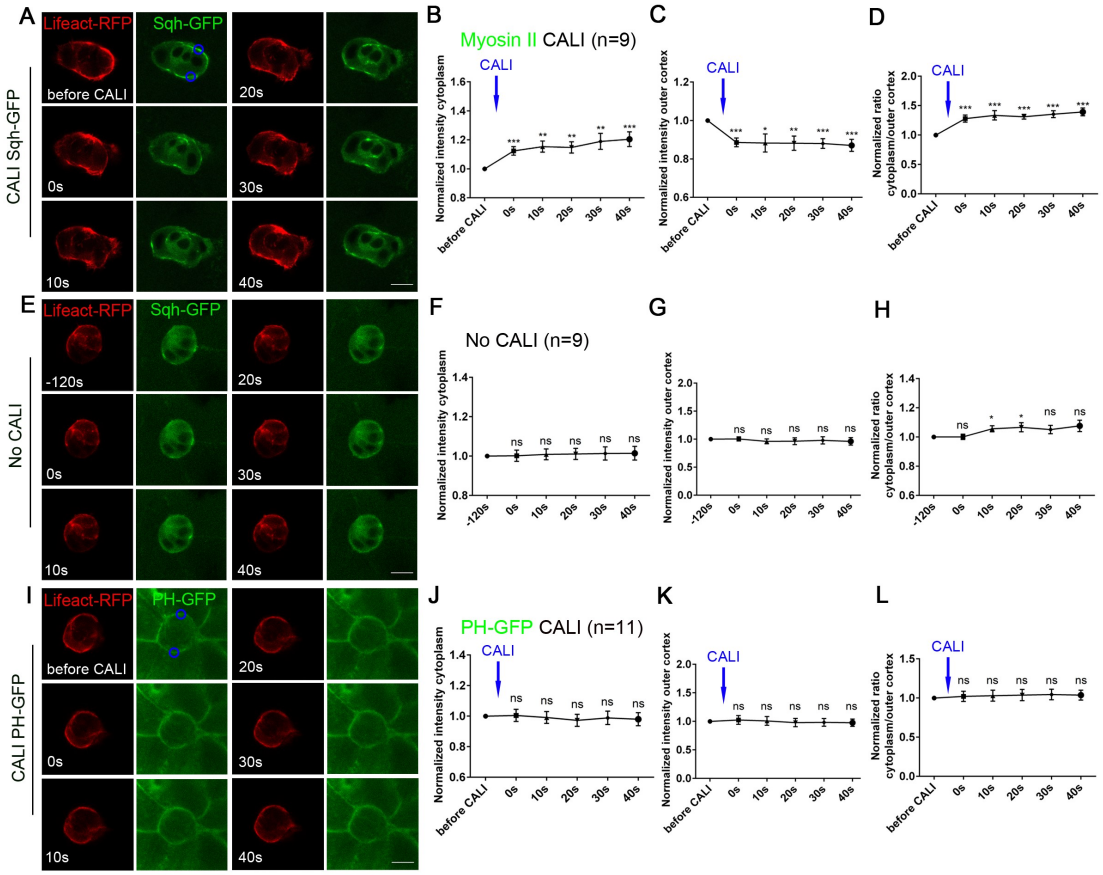

Figure S8. Local CALI of Sqh-GFP moderately alters the distribution of F-actin, Related to Figure 7. (**A-D**) Confocal images showing that F-actin (labeled with Lifeact-RFP) levels at the outer cortex moderately decrease while F-actin levels in the cytoplasm are moderately increased after Sqh-GFP CALI treatment (**A**). The results are quantified in (**B-D**) as normalized intensity of F-actin in cytoplasm, normalized intensity in outer cortex, and cytoplasmic F-actin/outer cortex F-actin ratio at different time points (n=9 BC clusters). (**E**) F-actin levels and distribution are not significantly changed without CALI treatment of Sqh-GFP. (**F-H**) Quantification of F-actin levels in the cytoplasm, outer cortex, and cytoplasmic F-actin/outer cortex F-actin ratio without CALI treatment (n=9). (**I**) F-actin levels and distribution are not significantly changed after PH-GFP CALI treatment. (**J-L**) Quantification of F-actin levels in the cytoplasm, outer cortex, and cytoplasmic F-actin/outer cortex F-actin ratio after CALI of PH-GFP (n=11). Two blue circles indicate regions of illumination. *, <0.05; **, P<0.01; ***, P<0.001; ns, not significant (Student's t-test); Data are represented as mean ± SEM. Scale bars: 10 μm.

Transparent methods

Drosophila genetics

Flies were cultured following standard procedures at 25℃ except for RNAi experiments (at 29℃). All strains were obtained from the Bloomington Drosophila Stock Center (BDSC), National Institute of Genetics Stock Center (Japan), Vienna Drosophila RNAi Center and Tsinghua University RNAi Stock Center, except for the followings: *E-cad-GFP* (Huang et al., 2009), *Sqh-mCherry* (Martin et al., 2009; Qin et al., 2017), *UAS-puc* (Ma et al., 2012), *UAS-PA-RacQ61L* (Wang et al., 2010), *UAS-PA-RacQ61L-C450M* (Wang et al., 2010), *UAS-RacFRET* (Wang et al., 2010), *UAS-aPKC-CAAX* (Lee et al., 2006), *UAS-moesin-mCherry* (gift from Dr. Xiaobo Wang). To perform flip-out experiments, *AyGal4;UAS* transgenes were crossed to *hs-FLP*. Newly enclosed flies were heat shocked in a 37℃ water bath for 5 minutes. For analysis of single-cell clones, mosaic clusters containing only one BC expressing GFP were used. *Drosophila* stocks obtained from public stock centers are listed below.

GENOTYPE	STOCK#	SOURCE
UAS-sqh RNAi	THU1223	Tsinghua University RNAi Stock Center (TURSC)
UAS-rok RNAi	THU1539	TURSC
UAS-rho1 RNAi	9910	Bloomington Drosophila Stock Center (BDSC)
UAS-aPKC RNAi	THU5841	TURSC
UAS-RacN17	6292	BDSC
UAS-GFP	1522	BDSC
UAS-Lifeact-GFP	35544	BDSC
UAS-Lifeact-RFP	58362	BDSC
UAS-arp2 RNAi	29944	Vienna Drosophila Research Center (VDRC)
UAS-arp3 RNAi	35260	VDRC
UAS-arp3 RNAi	7558R-1	National Institute of Genetics (NIG)
UAS-E-cad RNAi	27081	VDRC
UAS-moesin RNAi	33936	BDSC
UAS-moesin-DN	52234	BDSC
sqh^{AX3}*;sqh-GFP*	57144	BDSC

PH-GFP(PIP3 marker)	8164	BDSC
cdc42-mCherry	42237	BDSC
$rac1^{J11}rac2^{\triangle}mtl^{\triangle}$/+	6678	BDSC
$rac1^{J10}rac2^{\triangle}mtl^{\triangle}$/+	6679	BDSC

Immunostaining and microscopy

Ovary dissection was carried out in phosphate-buffered saline (PBS) and then fixed in devitellinizing buffer (7% formaldehyde) and heptane (Sigma) mixture (1:6) for 10 min(Zhang et al., 2011). After three washes in PBS, ovaries were incubated in PBT (PBS with 3% Triton X-100) and blocking solution (PBT, 10% goat serum) for 30 min and then stained overnight at 4°C. Primary antibodies were as followed: rabbit anti-phospho-Myosin II (3671S, 1:100, Cell Signaling), rabbit anti-PKCζ (C-20, 1:200, Santa Cruz), rat anti-E-cad (DCAD2, 1:50, DSHB), rabbit anti-Baz (1:400, gift from A. Wodarz), After washes in PBT, ovaries were incubated with secondary antibodies (1:200, Jackson ImmunoResearch) for 2 hours at room temperature. F-actin was labeled by Rhodamine-phalloidin (P1951, 1:200, Sigma)for 1 hour. Confocal images were obtained using a Leica TCS SP5 II or a Zeiss 880 microscope (with Airyscan technology) and images were processed by ImageJ and Imaris (Bitplane).

High resolution imaging of actin network.

Egg chambers were dissected in cold PBS medium. To avoid distortion or compression of BC cluster in the Z-axis, we used 2 coverslips (0.13-0.17mm thick) as bridges to mount egg chambers so that there is ample space in the z-axis to avoid compression of BC clusters and thus distortion of the actomyosin network on the cluster surface. High resolution images were captured using Zeiss 880 Airyscan mode, which employs an Airyscan detector consisting of 32 single detector elements. A maximum resolution of 120nm in the x-y plane can be achieved according to the manufacturer's description.

Live imaging and photomanipulation

Egg chambers were dissected and mounted for live imaging as described previously

(Prasad and Montell, 2007; Wang et al., 2018). A Leica SP5 II confocal microscope equipped with a HyD detector and a Zeiss 880 confocal microscope were used for live imaging.

For the PA-Rac photoactivation assay in Figures 4, 5 and S5, the 458 nm laser (set at 8% laser power) was used to illuminate a spot of 7μm in diameter. The photoactivation scan lasted about 30 s. The BCs were then imaged using a 561 nm laser. This series of steps was repeated for the duration of the time-lapse experiment. Photoactivation was carried out using Zeiss 880 confocal microscope.

Rac-FRET imaging and analysis were performed as described by Wang et al. (2010) and Wang et al. (2018)(Wang et al., 2018; Wang et al., 2010). Briefly, CFP and YFP images were collected simultaneously with the Leica TCS SP5 II confocal microscope, and then processed by Image J. A Gaussian smoothing filter was applied to both channels, background was then subtracted. The CFP images were used to create a binary mask with the background set to zero. The final images were generated from YFP/CFP ratios. The FRET index was calculated for the front or rear side of BC cluster by measuring the average intensity of FRET.

Chromophore-assisted laser inactivation (CALI)

CALI was performed on two GFP-fused proteins: Sqh-GFP and PH-GFP (pleckstrin-homology domain of Grp1 fused to GFP, used as a PIP3 probe). PH-GFP mainly localizes in the periphery of BC cluster and was used as a control. The *sqh-GFP* transgene is expressed in the background of the *sqh* null allele (heterozygous). CALI was performed with the Zeiss 880 confocal microscope, using a Plan-Apochromat 40x/1.3 Oil DIC M27 objective. For CALI, the laser power of the 488nm laser was set at 100% to maximize production of reactive oxygen species locally. But for image acquisition, GFP signals were acquired using 488nm laser at 3-4% laser power.

For Figure S2, CALI was performed at the rear side of Sqh-GFP or PH-GFP expressing BC clusters that were in the process of undergoing detachment from the anterior follicle epithelium. A 40x objective with x2 numerical zoom was used. The 488 nm laser was used to perform CALI. Two ROIs with the diameter of 3μm were chosen for illumination of Sqh-GFP or PH-GFP at 100% laser power. Parameters of CALI were as followed: illumination time, 5s; bidirectional scan; pinhole, 2.66AU; scan speed, 8 arbitrary units; iterations, 3-4. After CALI, a z-series of about 20 confocal sections was taken every 2 min for 1 hour, and these confocal images were subjected to maximum projection. Sqh-GFP labeled BCs without CALI and PH-GFP labeled BCs with CALI were used as controls.

For Figures 2F-2K, CALI was performed on Sqh-GFP or PH-GFP expressing BC clusters that have completed detachment from the anterior follicle epithelium and was undergoing migration between nurse cells. A 40x objective with x3 numerical zoom was used. Two ROIs with the diameter of 3nm near the periphery of lateral-positioned BCs were chosen for illumination of Sqh-GFP or PH-GFP at 100% laser power. The parameters of CALI are the same as described above except that the iterations are 8. Lifeact-RFP was used to label F-actin and follow the morphological changes of BC cluster. After CALI, a z-series was acquired every 5 minutes for 20 minutes.
For Figure 5, the parameters of CALI are the same as described above except that iterations of ROI illumination are 3-4.

For Figure S8, the parameters of CALI treatment are the same as described above except that iterations of ROI illumination are 6-8. After CALI, a single confocal section was taken every 10 seconds for 40 seconds.

Quantification of BC migration

For Figure S6E, BCs were labeled by expression of *UAS-GFP* using the *slbo-Gal4* driver. To quantify BC migration, stage 10 egg chambers were used. Depending on the positioning of the cluster along the migratory route (between the anterior tip of the

egg chamber and the oocyte border), the extent of BC migration was measured and categorized into five classes: 0% (no migration), 25%, 50%, 75% and 100% (arriving at border). Migration index (M.I.) was then calculated according to the following formula to evaluate migratory ability, as described previously(Assaker et al., 2010):

$$M.I.=\frac{1*n(100\%)+0.75*n(75\%)+0.5*n(50\%)+0.25*n(25\%)+0*n(0\%)}{N}$$

n(%) represents the number of BC clusters that have completed certain % of migratory route at stage 10. N is the total number of stage 10 egg chambers examined.

Measurement of protrusions

For Figures 2A-2C; Figures 7A and 7B; and Figures S6D, S6F and S6H, Rhodamine-phalloidin was used to label F-actin. For Figures 7C-7G; Figures S6A and S6B, GFP driven by *slbo-Gal4* was used to outline the morphology of BCs. A z-series of confocal sections was first taken for each BC cluster. After maximum projection, protrusions were measured and determined by the distance from the protrusion tip to the boundary between the basal region of protrusion and cell body. Those longer than 3μm in length and 3μm in width were qualified as protrusions.

For Figure S4, Lifeact-RFP driven by *slbo-Gal4* and Sqh-GFP were used to label protrusions. The length of protrusion was measured as described above. The distance from initial position for the Myosin II patches was measured as the linear distance between the centers of Myosin II patches at the initial time point and the later time points.

For Figures 7H-7J, GFP driven by *slbo-Gal4* was used to outline the morphology of BCs expressing *aPKC-CAAX* and *Sqh RNAi*. Olympus BX51 fluorescent microscope was used to acquire the images. Protrusions longer than 10 μm in length and 7 μm in width were counted as huge protrusions.

To determine the position of protrusions in Figure 1F, 2A and 2B, 7H-7J, S6A and

S6B, S6D, S6F and S6H, we divided BC cluster into four quadrants: one front, two lateral, one rear (as shown in Figure 2D). Protrusions extended from the front quadrant were defined as leading protrusion, whereas those extended from lateral or rear sides were considered as ectopic protrusions. When two or more protrusions were situated at similar positions around the front of the cluster, the larger one was designated the leading protrusion. If two protrusions were similar in size, the one situated more toward the front or leading position was designated the leading protrusion.

For live imaging in Figures 2F-2N, Figures 4A-4C, and Figures 5A-5D, Lifeact-RFP (CALI assay) or PA-Rac-mCherry (Rac photoactivation or Rac photoactivation + CALI assay) was used to label protrusions. A z-series of about 25 confocal sections was taken for each BC cluster at each time point. For CALI assay, the confocal sections were subjected to 3D reconstruction using Zen software (Zeiss), and then protrusions were determined and measured by viewing BCs from different angles. For Rac photoactivation (or Rac photoactivation + CALI） assay, confocal images were subjected to maximum projection. The length and width of each protrusion were measured and determined from the final projected images. Protrusions that are at least 3μm in length (from tip to base) and 3μm in width at the base were counted. Confocal images were obtained with a Leica TCS SP5 II or a Zeiss 880 confocal microscope.

Quantification of fluorescence intensity

Image J was used to measure FI (Fluorescence Intensity). A region of interest was first chosen and outlined. Then average fluorescence intensity of the outlined region was determined, and this value was used as the FI. To measure the outer cortex/cytoplasm ratio for Figures S6G, S6J and Figure S7C, a freehand line was drawn along the periphery of BC cluster as the outer cortex region, and an area of cytoplasm was chosen as the cytoplasmic region. FI (Fluorescence Intensity) was measured by Image J for each region; the outer cortex/cytoplasm ratios were calculated as: outer cortex FI/cytoplasm FI.

For Figures 6C, 6D, 6F, 6H and S8, the ways of measuring fluorescence intensity are the same as described above except that all the areas of cytoplasm including PCs were chosen as the cytoplasmic regions. For Figure S8, the fluorescent intensities of Lifeact-RFP measured right before CALI (at the time point of "before CALI") were used for normalization.

To measure the junction/cytoplasm ratio for Figures 6B and S1E, a freehand line was drawn along the apical junctions of BC cluster as the junction region, and an area of cytoplasm was chosen as the cytoplasmic region. FI (Fluorescence Intensity) was measured by Image J for each region; the junction/cytoplasm ratios were calculated as: junction FI/cytoplasm FI.

Quantification of Myosin II patches and spots

For Figure S5B, Sqh-GFP was used to label Myosin II and Lifeact-RFP was used to label F-actin. First, a z-series of confocal sections was taken for each BC cluster every 2 minutes for about 1 hour, and these confocal images were subjected to maximum projection. The area of Lifeact-RFP-labeled protrusions was determined as the region spanning from the protrusion tip to the boundary between the basal region of protrusion and cell body. To determine and measure the area of Myosin II patches, the threshold option in the Image J software was used to mark the patches outlines. In brief, all the Sqh-GFP images (green channel) from time-lapse movies were first processed with Gaussian smoothing filter, then a threshold option was applied with filtered parameter set manually to mark all the Myosin II patches. Finally, these areas were selected and measured as the areas of Myosin II patches.

To quantify the number of Myosin II patches and Myosin II spots in Figure S5G and S5H, A 40x objective with x4 numerical zoom was used and the size of confocal images captured was 512x512 pixels. We used "analyze particles" option in Image J software to label and calculate the number of patches or spots. All the images of

Sqh-GFP channel from one sample were first processed with smoothing filter, then a color threshold option was applied to each image with filtered parameter set manually to reveal all the strong Myosin II signals. Then we used the "analyze particles" option to label patches or spots. The parameter we set for patches is 200-infinity pixel units, and 10-200 pixel units for spots. Circularity is 0-1.

Drug treatments

Egg chambers were dissected in live medium and then evenly divided into 2 or 3 groups. Each group was incubated in Latrunculin A (2 μM in live imaging medium, Invitrogen), or Jasp (2 μM in live imaging medium, Invitrogen), or DMSO (2 μM in live imaging medium, Sangon) for 1.5 hours before fixation and mounting. The live imaging medium was as described previously(Prasad and Montell, 2007; Wang et al., 2018).

Statistical analysis

Statistical analyses were performed with GraphPad Prism, version 5.01. Statistical comparisons of means were made using the unpaired two-tailed Student's t-test. $P<0.05$ was considered statistically significant.

Supplemental references

Assaker, G., Ramel, D., Wculek, S.K., Gonzalez-Gaitan, M., and Emery, G. (2010). Spatial restriction of receptor tyrosine kinase activity through a polarized endocytic cycle controls border cell migration. Proceedings of the National Academy of Sciences of the United States of America *107*, 22558-22563.

Huang, J., Zhou, W., Dong, W., Watson, A.M., and Hong, Y. (2009). From the Cover: Directed, efficient, and versatile modifications of the Drosophila genome by genomic engineering. Proceedings of the National Academy of Sciences of the United States of America *106*, 8284-8289.

Lee, C.Y., Robinson, K.J., and Doe, C.Q. (2006). Lgl, Pins and aPKC regulate neuroblast self-renewal versus differentiation. Nature *439*, 594-598.

Ma, X., Huang, J., Yang, L., Yang, Y., Li, W., and Xue, L. (2012). NOPO modulates Egr-induced JNK-independent cell death in Drosophila. Cell research *22*, 425-431.

Martin, A.C., Kaschube, M., and Wieschaus, E.F. (2009). Pulsed contractions of an actin-myosin network drive apical constriction. Nature *457*, 495-499.

Prasad, M., and Montell, D.J. (2007). Cellular and molecular mechanisms of border cell migration analyzed using time-lapse live-cell imaging. Developmental cell *12*, 997-1005.

Qin, X., Park, B.O., Liu, J., Chen, B., Choesmel-Cadamuro, V., Belguise, K., Heo, W.D., and Wang, X.

(2017). Cell-matrix adhesion and cell-cell adhesion differentially control basal myosin oscillation and Drosophila egg chamber elongation. Nature communications *8*, 14708.

Wang, H., Qiu, Z., Xu, Z., Chen, S.J., Luo, J., Wang, X., and Chen, J. (2018). aPKC is a key polarity molecule coordinating the function of three distinct cell polarities during collective migration. Development.

Wang, X., He, L., Wu, Y.I., Hahn, K.M., and Montell, D.J. (2010). Light-mediated activation reveals a key role for Rac in collective guidance of cell movement in vivo. Nature cell biology *12*, 591-597.

Zhang, L., Luo, J., Wan, P., Wu, J., Laski, F., and Chen, J. (2011). Regulation of cofilin phosphorylation and asymmetry in collective cell migration during morphogenesis. Development *138*, 455-464.